FU JEN STUDIES

NATURAL SCIENCES

NO. 15   1981

CONTENTS

FU JEN UNIVERSITY

TAIPEI, TAIWAN, REPUBLIC OF CHINA

SURFACE OF REVOLUTION WITH PRESCRIBED GAUSSIAN CURVATURE

Yi-Ching Yen

1. THEORY

In this note we study a surface of revolution in E^3. For a given continuous function K which represents the Gaussian curvature of a surface of revolution, we will find its profile curve by an elementary differential equation. The discussions and the figures about the surfaces of revolution of K=constant, which are the particular cases of this note, can be seen in some text books[1,2] of differential geometry.

Let $\alpha(u) = (g(u), h(u), 0)$, $u \in I$, be any C^2-curve parameterized by its arc length u, and the domain of definition I is any open interval of real number containing 0. The surface of revolution generated by revolving α about x-axis takes the form

$$(g(u), h(u) \cos v, h(u) \sin v), \qquad u \in I, \quad v \in [0, 2\pi]. \qquad (1)$$

Since $g'^2 + h'^2 = 1$, we have

$$E = 1, \quad F = 0, \quad G = h^2;$$
$$l = -g' h'' + g'' h', \quad m = 0, \quad n = gh. \qquad (2)$$

Therefore

$$K = \frac{g'h(-g' h'' + g'' h')}{h^2} = -\frac{h''}{h}. \qquad (3)$$

Thus we have a 2nd order linear differential equation

$$h''(u) + K(u) h(u) = 0, \qquad u \in I. \qquad (4)$$

Let $h = e^z$, then (2) becomes

$$e^z(z''(u) + z'^2(u) + K(u)) = 0, \qquad (5)$$

which implies

$$z''(u) + z'^2(u) + K(u) = 0. \qquad u \in I. \qquad (6)$$

Put $z' = w$, then (3) becomes a Ricatti differential equation

$$w'(u) + w^2(u) + K(u) = 0, \qquad u \in I. \tag{7}$$

which has the general solution

$$w(u) = \frac{c_1 f_1(u) + f_2(u)}{c_1 f_3(u) + f_4(u)} = z'(u), \quad c_1: \text{arbitrary constant,}$$

$$f_i \in C^1, \quad (i = 1, 2, 3, 4) \text{ in } I. \tag{8}$$

Thus,

$$h(u) = e^{z(u)} = c_2 \exp \int_0^u \frac{c_1 f_1(t) + f_2(t)}{c_1 f_3(t) + f_4(t)} \, dt, \qquad u \in I,$$

c_2: arbitrary constant.
$$\tag{9}$$

g is obtained by the integration

$$g(u) = \int_0^u (1 - h'^2(t))^{1/2} \, dt + c_3$$

$$= \int_0^u \left\{ 1 - c_2^2 \left(\exp 2 \int_0^u \frac{c_1 f_1(t) + f_2(t)}{c_1 f_3(t) + f_4(t)} \, dt \right) \right.$$

$$\left. \cdot \left(\frac{c_1 f_1(u) + f_2(u)}{c_1 f_3(u) + f_4(u)} \right)^2 \right\}^{1/2} dt + c_3, \qquad u \in I. \tag{10}$$

Thus we have a family of profile curves which is denoted by

$$\alpha(u) = X(u, K(u), c_1, c_2, c_3)$$

$$= \left(\int_0^u \left\{ 1 - c_2^2 \left(\exp 2 \int_0^u \frac{c_1 f_1(t) + f_2(t)}{c_1 f_3(t) + f_4(t)} \, dt \right) \right. \right.$$

$$\left. \cdot \left(\frac{c_1 f_1(u) + f_2(u)}{c_1 f_3(u) + f_4(u)} \right)^2 \right\}^{1/2} dt$$

$$+ c_3, \; c_2 \exp \int_0^u \frac{c_1 f_1(t) + f_2(t)}{c_1 f_3(t) + f_4(t)} \, dt, \; 0 \bigg), \qquad u \in I.$$

c_1, c_2, c_3: arbitrary constants.
$$\tag{11}$$

Thus we have proved

Theorem. Let $\alpha(u) = (g(u), h(u), 0)$ $(u \in I)$ be the profile curve, parameterized by the arc length u, of a surface of revolution whose Gaussian curvature at the point $(g(u), h(u) \cos v, h(u) \sin v)$, $u \in I$, $v \in [0, 2\pi]$, is given by $K(u)$, then $X(u, K(u), c_1, c_2, c_3)$ is the required profile curve $\forall u \in I$.

Hence for a given K, we can construct many surfaces admitting K as the Gaussian curvature.

2. TWO EXAMPLES

i) Let $K(u) = 1 - u^2$, then we have a solution for h as $h(u) = e^{-u^2/2}$, and $g(u) = \int_0^u \sqrt{1 - t^2 e^{-t^2}}\, dt$. The profile curve is:
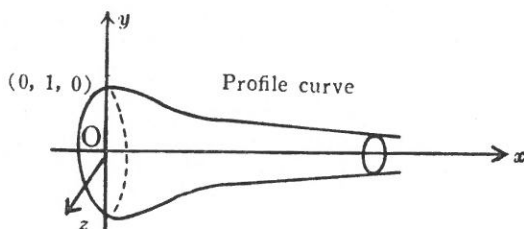
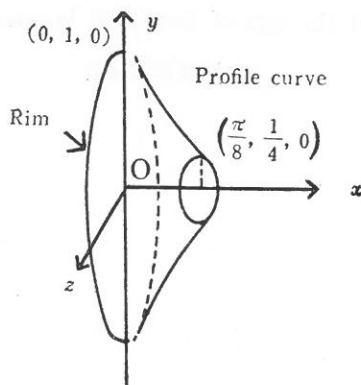ii) Let $K(u) = -1/u^2$, then $\exists$ a solution for h as $h(u) = u^2$, and

$$g(u) = \int_0^u \sqrt{1 - 4t^2}\, dt$$
$$= \frac{u}{4}\sqrt{1 - 4u^2} + \frac{1}{4}\sin^{-1} 2u.$$

The profile curve is shown as below:

REFERENCES

(1) Klingenberg, W., *A Course in Differential Geometry*, New York, Springer Verlag, 1978.
(2) O'Neill, B., *Elementary Differential Geometry*, New York, Academic Press. 1966.

"God made the integers,
and all the rest is the work of man."

LEOPOLD KRONECKER (1823–1891)

"The golden age of mathematics—
that was not the age of Euclid, it is ours."

C. J. KEYSER

THE SPIN EXCITATION OF THE MULTIPLE SPIN DENSITY WAVE OF THE γ-Mn SYSTEM

Sheau-Huey Chia

ABSTRACT

We investigate the theorectical structure of the multiple spin density wave of the γ-Mn system and sucessfully lay down the framework for the calculation of the excitation spectrum of such a system. The dispersion relation for the spin excitation is explicitly calculated.

1. INTRODUCTION

The transition metals are well known for their magnetic properties. Apart from the ferromagnetism of Fe, Ni and Co, several of these metals and alloys have antiferromagnetic structures. The magnetic properties of these metals can be described by a spacially oscillating magnetic moment on an atomic scale. This oscillating moment, whose period is usually denoted by $\vec{Q}$, is called the spin density wave (SDW). If the oscillation is commensurate with the lattice, there will be a reduction in the symmetry and the one-particle states can still be labelled by distinct wave vectors in a reduced Brillouin zone (BZ).

There have been many ways in constructing the spin density wave state. Slater[1], Matsubara[2] and des Cloiseaux[3] considered a two sublattice model and paired the electrons which have the same spin with one from each of the sublattices (This model applies only to the commensurate two-sublattice case). Later Overhauser[4] and Fedders and Martin[5] paired electrons with opposite spins. Morris and Cornwall[6] approached the problem by choosing a different quantization axis at each site. All these apparantly distinct approaches were shown by Young[7] to be equivalent in the case of a simply commensurate SDW. He found that the essential pairing between wave-vectors differ by $\vec{Q} = 2\pi/a(0, 0, 1)$.

It is possible that more than one such pairing occurs, so that the antiferromagnetic state consists of several SDW's. Indeed, Endo and Ishikawa[8] proposed in 1971 that the spin configuration in the magnetic phase of γ-Fe Mn alloy with the valence electron number between 7.4 and 7.7 is noncollinear; the four spins in a unit cell are, in fact, pointing toward four different tetrahedral directions. In that case, we shall have four interpenetrating simple cubic (SC) magnetic sublattices and the spacial variation of the spin is described in terms of the multiple spin density wave (MSDW) state with wavevectors $\vec{Q}_1 = 2\pi/a(0, 0, 1)$, $\vec{Q}_2 = 2\pi/a(1, 0, 0)$, $\vec{Q}_3 = 2\pi/a(0, 1, 0)$ as $\vec{S}(\vec{r}) = S/\sqrt{3} \, (\hat{z} \, e^{i \vec{Q}_1 \cdot \vec{r}} + \hat{x} \, e^{i \vec{Q}_2 \cdot \vec{r}} + \hat{y} \, e^{i \vec{Q}_3 \cdot \vec{r}})$.

There had been very little theoretical work done on the MSDW state, in spite of the fact that Sato and Maki[9] did try to investigate such state by employing an extended two-band model. The purpose of this paper is to construct the appropriate quasi-particle state and to study the spin excitation in this MSDW state.

We divide our paper into five sections. In section 2, we examine the reduced Brillouin Zone of the metal γ-Mn and construct the density matrix for the MSDW state from the spin configuration. In section 3, we lay down the framework of obtaining the quasi-particle states by diagonalizing the one-band Hubbard Hamiltonian in the Hartree-Fock approximation. In the fourth section we derive the dispersion relation for the spin excitations. The last section gives the conclusions. We also include three appendices at the end of the paper.

2. THE REDUCED BRILLOUIN ZONE AND THE DENSITY MATRIX

Let us consider a simple one-band, itinerant antiferromagnetic γ-Mn system, it has a fcc lattice structure and the reciprocal lattice is a truncated octahedron. The translational lattice vectors and the reciprocal lattice vectors are

$$\vec{R} = n_1 \vec{a} + n_2 \vec{b} + n_3 \vec{c}$$

with

$$\vec{a} = a/2(1, 1, 0)$$
$$\vec{b} = a/2(0, 1, 1)$$
$$\vec{c} = a/2(1, 0, 1)$$

and

$$\vec{G} = h\vec{A} + k\vec{B} + 1\vec{C}$$

with

$$\vec{A} = 2\pi/a(1, 1, -1)$$
$$\vec{B} = 2\pi/a(-1, 1, 1) \tag{2-1}$$
$$\vec{C} = 2\pi/a(1, -1, 1)$$

The spin configuration for the MSDW state and the translational lattice vectors of the corresponding sublattices are respectively (see Fig. 1):
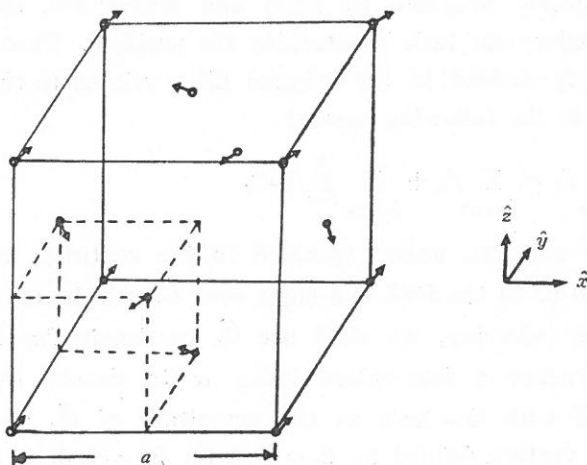

Fig. 1. The spin configuration for the multiple SDW state. The unit cell is now the full $a \times a \times a$ cube with the spins directed towards the center of the cubic cell indicated by the dashed lines.

corner,

$$\hat{e}_{11} = 1/\sqrt{3}\,(1, 1, 1), \qquad \vec{R}_1 = a(n_1, n_2, n_3)$$

bottom center,

$$\hat{e}_{21} = 1/\sqrt{3}\,(-1, -1, 1), \quad \vec{R}_2 = a\left(n_1 + \frac{1}{2}, n_2 + \frac{1}{2}, n_3\right) \tag{2-2}$$

middle sided,

$$\hat{e}_{31} = 1/\sqrt{3}\,(1,\,-1,\,-1), \quad \vec{R}_3 = a\left(n_1,\,n_2 + \frac{1}{2},\,n_3 + \frac{1}{2}\right)$$

middle front,

$$\hat{e}_{41} = 1/\sqrt{3}\,(-1,\,1,\,-1), \quad \vec{R}_4 = a\left(n_1 + \frac{1}{2},\,n_2,\,n_3 + \frac{1}{2}\right)$$

They form four interpenetrating simple cubes (SC). The reciprocal lattice is also a cube, and the reduced BZ is a cube embedded into the original BZ, which has a volume one-fourth of the fcc one (see Appendix A).

In Appendix B, we show that any wave vector $\vec{k}$ in the original BZ can be transformed back to the reduced BZ (RBZ) by using the three vectors $\vec{Q}_1 = 2\pi/a(0,\,0,\,1)$, $\vec{Q}_2 = 2\pi/a(1,\,0,\,0)$, $\vec{Q}_3 = 2\pi/a(0,\,1,\,0)$. The above three vectors coincide, fortunately, with the wave vectors of the MSDW proposed by Endo and Ishikawa[8], and this will greatly reduce our task in attacking the problem. Then any sum of quantity $f_{\vec{k}}$ defined in the original BZ is related to the sums over the RBZ in the following manner

$$\sum_{\vec{k}\in\text{BZ}} f_{\vec{k}} = \sum_{\vec{k}\in\text{RBZ}} f_{\vec{k}} + \sum_{\vec{k}\in\text{RBZ}} \sum_{i=1}^{3} f_{\vec{k}+\vec{Q}_i} \tag{2-3}$$

From now on, unless specified to the contrary, all $\vec{k}$'s will be deemed to be in the RBZ and sums over $\vec{k}$'s will be over the RBZ.

In the following, we shall use $\vec{Q}_0$ to denote $2\pi/a(0,\,0,\,0)$ and shall introduce a four-valued index α to denote each $\vec{Q}_\alpha$'s as $\vec{Q}_\alpha = \hat{n}_\alpha Q$ with $Q = 2\pi/a$ as the magnitude of $\vec{Q}_\alpha$ and $\hat{n}_\alpha$ as the direction vectors defined as $\hat{n}_0 = (0,\,0,\,0)$, $\hat{n}_1 = (0,\,0,\,1)$, $\hat{n}_2 = (1,\,0,\,0)$ and $\hat{n}_3 = (0,\,1,\,0)$. Because $\vec{k} + \vec{Q}_\alpha$ will keep k within or will take it out of the RBZ (but still inside the original BZ), the sum or difference of the Q_α's will be

$$\vec{Q}_{\alpha_1} \pm \vec{Q}_{\alpha_2} = \sum_{\alpha_3} (\vec{Q}_{\alpha_3} \pm \vec{G})\,\varepsilon_{\alpha_1\alpha_2\alpha_3} \tag{2-4}$$

where $\vec{G}$ is an appropriate reciprocal lattice vector, and $\varepsilon_{\alpha_1\alpha_2\alpha_3}$ is the completely antisymmetric tensor of third rank. And this will give the following addition rules for the α's

$$\alpha_1 \pm \alpha_2 = \alpha_3\, e_{\alpha_1\alpha_2\alpha_3} \tag{2-5}$$

We shall see that the above addition rules are very important in our subsequent discussions.

The spin density vector is defined as

$$\vec{S}(\vec{r}) = 1/2\Psi^\dagger_{\sigma_1}(\vec{r})\,\vec{\sigma}_{\sigma_1\sigma_2}\Psi_{\sigma_2}(\vec{r})$$

$$= 1/2 \sum_{\vec{k}_1,\vec{k}_2\in\mathrm{BZ}} \phi_{\vec{k}_1}(\vec{r})\,\phi^*_{\vec{k}_2}(\vec{r})\,\vec{\sigma}_{\sigma_1\sigma_2}\,\rho^{\sigma_1\,\sigma_2}_{\vec{k}_1\,\vec{k}_2} \tag{2-6}$$

where we have adopted the convention that all numerically subscripted variables are summed over and all wave vectors are modulo a reciprocal lattice vectors. $\rho^{\sigma\,\sigma'}_{\vec{k}\,\vec{k}'} = \langle a^+_{\vec{k}'\,\sigma'}\, a_{\vec{k}\sigma}\rangle$ is the density matrix with $\vec{\sigma}_{\sigma\sigma'}$ as the Pauli spin matrix, and σ labels the spin state. $\phi_{\vec{k}}(\vec{r})$ is the Bloch function. Writing out the components of the spin density will look like

$$S^x(\vec{r}) = 1/2\ \phi_{\vec{k}_1}(\vec{r})\,\phi^*_{\vec{k}_2}(\vec{r})\ (\rho^{\uparrow\ \downarrow}_{\vec{k}_1\ \vec{k}_2} + \rho^{\downarrow\ \uparrow}_{\vec{k}_1\ \vec{k}_2})$$

$$S^y(\vec{r}) = 1/2i\ \phi_{\vec{k}_1}(\vec{r})\,\phi^*_{\vec{k}_2}(\vec{r})\ (\rho^{\uparrow\ \downarrow}_{\vec{k}_1\ \vec{k}_2} - \rho^{\downarrow\ \uparrow}_{\vec{k}_1\ \vec{k}_2}) \tag{2-7}$$

$$S^z(\vec{r}) = 1/2\ \phi_{\vec{k}_1}(\vec{r})\,\phi^*_{\vec{k}_2}(\vec{r})\ (\rho^{\uparrow\ \uparrow}_{\vec{k}_1\ \vec{k}_2} - \rho^{\downarrow\ \downarrow}_{\vec{k}_1\ \vec{k}_2})$$

The symbols $\uparrow$ and $\downarrow$ denote respectively spin up and spin down states.

There are some relations among the density matrices because of the particular spin configurations as described by Eq (2-2). We shall leave the derivation of these relations in Appendix C, and shall just write them down in the following two equations,

$$\rho^{\sigma\,\sigma'}_{\vec{k}\,\vec{k}'} = \delta_{\sigma'\sigma}(\rho^{\sigma\,\sigma}_{\vec{k}\,\vec{k}}\,\delta_{\vec{k}'\,\vec{k}} + \sigma\,\rho^{\sigma\,\sigma}_{\vec{k}\,\vec{k}+\vec{Q}_1}\,\delta_{\vec{k}'\,\vec{k}+\vec{Q}_1})$$

$$+ \delta_{\sigma'\,\bar{\sigma}}(\rho^{\sigma\,\bar{\sigma}}_{\vec{k}\,\vec{k}+\vec{Q}_2}\,\delta_{\vec{k}'\,\vec{k}+\vec{Q}_2} + \sigma\,\rho^{\sigma\,\bar{\sigma}}_{\vec{k}\,\vec{k}+\vec{Q}_3}\,\delta_{\vec{k}'\,\vec{k}+\vec{Q}_3})\,, \tag{2-8}$$

and

$$\sum_{\vec{k}\in\mathrm{BZ}} \rho^{\uparrow\ \uparrow}_{\vec{k}\ \vec{k}+\vec{Q}_1} = \sum \rho^{\uparrow\ \downarrow}_{\vec{k}\ \vec{k}+\vec{Q}_2} = (-i)\sum \rho^{\uparrow\ \downarrow}_{\vec{k}\ \vec{k}+\vec{Q}_3}\,, \tag{2-9}$$

where $\bar{\sigma}$ denotes the spin state opposite to that labelled by σ.

The above two relations can also be expressed in terms of Q's and the wave vectors in the RBZ by using the α notation:

$$\rho_{\vec{k}}^{\alpha\sigma}{}_{\vec{k}'}^{\alpha'\sigma'} = \delta_{\vec{k}\vec{k}'}\,\delta_{\sigma'\sigma}(\rho_{\vec{k}}^{\alpha\sigma}{}_{\vec{k}}^{\alpha\sigma}\delta_{\alpha'\alpha} + \sigma\rho_{\vec{k}}^{\alpha\sigma}{}_{\vec{k}}^{\alpha+1\sigma}\delta_{\alpha'\alpha+1})$$

$$+ \delta_{\vec{k}\vec{k}'}\,\delta_{\sigma'\bar{\sigma}}(\rho_{\vec{k}}^{\alpha\sigma}{}_{\vec{k}}^{\alpha+2\bar{\sigma}}\delta_{\alpha'\alpha+2} + \sigma\rho_{\vec{k}}^{\alpha\sigma}{}_{\vec{k}}^{\alpha+3\bar{\sigma}}\delta_{\alpha'\alpha+3}) \quad (2\text{--}10)$$

and

$$\sum_{\alpha_1\vec{k}_1}\rho_{\vec{k}_1}^{\alpha_1\uparrow}{}_{\vec{k}_1}^{\alpha_1+1\uparrow} = \sum_{\alpha_1\vec{k}_1}\rho_{\vec{k}_1}^{\alpha_1\uparrow}{}_{\vec{k}_1}^{\alpha_1+2\downarrow} = \sum_{\alpha_1\vec{k}_1}(-i)\,\rho_{\vec{k}_1}^{\alpha_1\uparrow}{}_{\vec{k}_1}^{\alpha_1+3\downarrow} \quad (2\text{--}11)$$

3. THE QUASI-PARTICLE STATES

The one-band Hubbard Hamiltonian[10] for this MSDW system is

$$\hat{H} = \hat{T} + \hat{V}$$

$$\hat{T} = \tilde{\varepsilon}_{\vec{k}_1}\,a_{\vec{k}_1\sigma_1}^{\dagger}\,a_{k_1\sigma_1} \quad (3\text{--}1)$$

$$\hat{V} = 1/2V\,a_{\vec{k}_1\sigma_1}^{\dagger}\,a_{\vec{k}_2\sigma_2}^{\dagger}\,a_{\vec{k}_4\bar{\sigma}_1}\,a_{\vec{k}_3\bar{\sigma}_1}\,\delta_{\vec{k}_1+\vec{k}_2,\vec{k}_3+\vec{k}} \quad (3\text{--}2)$$

And in the sub-band notation, the kinetic energy operator takes the form of

$$\hat{T} = \tilde{\varepsilon}_{\vec{k}_1}^{\alpha_1}\,a_{\vec{k}_1\,\sigma_1}^{\dagger\alpha_1}\,a_{\vec{k}_1\,\sigma_1}^{\alpha_1} \quad (3\text{--}3)$$

In the Hartree-Fock approximation, the antiferromagnetic (AF) interaction term $\hat{V}_{AF}$ can be written as

$$\hat{V}_{AF} = V(\rho_{\vec{k}_2}^{\alpha_3\bar{\sigma}_1}{}_{\vec{k}_2}^{\alpha_2\bar{\sigma}_1}\,a_{\vec{k}_2\sigma_1}^{\dagger\alpha_1}\,a_{\vec{k}_1\sigma_1}^{\alpha_4}$$

$$- \rho_{\vec{k}_2}^{\alpha_3\sigma_1}{}_{\vec{k}_2}^{\alpha_2\bar{\sigma}_1}\,a_{\vec{k}_1\sigma_1}^{\dagger\alpha_1}\,a_{\vec{k}_1\bar{\sigma}_1}^{\alpha_4})\,\delta_{\alpha_1+\alpha_2,\alpha_3+\alpha_4} \quad (3\text{--}4)$$

By plugging into Eqs (2–10), (2–11) and by using Eq (2–5) we simplify $\hat{V}_{AF}$ in Eq (3–4) to

$$\hat{V}_{AF} = \nu^{\sigma_1}a_{\vec{k}_1\sigma_1}^{\dagger\alpha_1}\,a_{\vec{k}_1\sigma_1}^{\alpha_1} - \sigma_1 g\,a_{\vec{k}_1\sigma_1}^{\dagger\alpha_1}\,a_{\vec{k}_1\sigma_1}^{\alpha_1+1}$$

$$- g\,a_{\vec{k}_1\sigma_1}^{\dagger\alpha_1}\,a_{\vec{k}_1\bar{\sigma}_1}^{\alpha_1+2} - i\,\sigma_1 g\,a_{\vec{k}_1\sigma_1}^{\dagger\alpha_1}\,a_{\vec{k}_1\bar{\sigma}_1}^{\alpha_1+2} \quad (3\text{--}5)$$

where

$$\nu^{\sigma} = V\,\rho_{\vec{k}_1}^{\alpha_1\bar{\sigma}}{}_{\vec{k}_1}^{\alpha_1\bar{\sigma}} \quad (3\text{--}6)$$

is the usual self-consistent HF potential present even in the non-AF state. And g is the self consistent gap parameter of the AF state which is defined as

$$g = V \rho_{\vec{k}_1 \, \vec{k}_1}^{\alpha_1 \uparrow \, \alpha_1 + 1 \uparrow} = V \rho_{\vec{k}_1 \, \vec{k}_1}^{\alpha_1 \uparrow \, \alpha_1 + 2 \downarrow}$$

$$= (-i) \, V \rho_{\vec{k}_1 \, \vec{k}_1}^{\alpha_1 \uparrow \, \alpha_1 + 3 \downarrow} \tag{3-7}$$

From Eq (3-3) and Eq (3-5), the linearized Hamiltonian becomes

$$\hat{H}_{AF}^0 = \text{const.} + (\tilde{\varepsilon}_{\vec{k}_1}^{\alpha_1} + \nu^{\sigma_1}) \, a_{\vec{k}_1 \sigma_1}^{\dagger \alpha_1} \, a_{\vec{k}_1 \sigma_1}^{\alpha_1} - \sigma_1 \, g \, a_{\vec{k}_1 \sigma_1}^{\dagger \alpha_1} \, a_{\vec{k}_1 \sigma_1}^{\alpha_1 + 1}$$

$$- g \, a_{\vec{k}_1 \sigma_1}^{\dagger \alpha_1} \, a_{\vec{k}_1 \bar{\sigma}_1}^{\alpha_2 + 2} - i \, \sigma_1 \, g \, a_{\vec{k}_1 \sigma_1}^{\dagger \alpha_1} \, a_{\vec{k}_1 \bar{\sigma}_1}^{\alpha_1 + 3} \tag{3-8}$$

There first two terms appearing in the above equation are the paramagnetic energies and they are diagonalized in both the momentum space and the spin space. We shall therefore write them as $H_{p \vec{k} \sigma}^{\alpha} \, (= \tilde{\varepsilon}_{\vec{k}}^{\alpha} + \nu^{\sigma})$ or simply H_p^{α}; this Hamiltonian is independent of σ.

We may write the Hamiltonian $\hat{H}_{AF}$ in the matrix form as

$$\hat{H}_{AF}^0 = (a_{\vec{k} \uparrow}^{\dagger 0}, \, a_{\vec{k} \uparrow}^{\dagger 1}, \, a_{\vec{k} \downarrow}^{\dagger 2}, \, a_{\vec{k} \downarrow}^{\dagger 3}, \, a_{\vec{k} \downarrow}^{\dagger 0}, \, a_{\vec{k} \downarrow}^{\dagger 1}, \, a_{\vec{k} \uparrow}^{\dagger 2}, \, a_{\vec{k} \uparrow}^{\dagger 3})$$

$$\times
\begin{bmatrix}
\begin{array}{cccc|cccc}
H_p^0 & -g & -g & -ig & & & & \\
-g & H_p^1 & -ig & -g & & & 0 & \\
+g & ig & H_p^2 & +g & & & & \\
ig & -g & g & H_p^3 & & & & \\
\hline
 & & & & H_p^0 & +g & -g & ig \\
 & & 0 & & +g & H_p^1 & ig & -g \\
 & & & & -g & -ig & H_p^2 & -g \\
 & & & & -ig & -g & -g & H_p^3
\end{array}
\end{bmatrix}
\times
\begin{bmatrix}
a_{\vec{k} \uparrow}^0 \\
a_{\vec{k} \uparrow}^1 \\
a_{\vec{k} \downarrow}^2 \\
a_{\vec{k} \downarrow}^3 \\
a_{\vec{k} \downarrow}^0 \\
a_{\vec{k} \downarrow}^1 \\
a_{\vec{k} \uparrow}^2 \\
a_{\vec{k} \uparrow}^3
\end{bmatrix}
\tag{3-9}$$

It contains two 4×4 block matrices which are related by a similar transformation effected by a 4×4 matrix $S = \begin{pmatrix} A & 0 \\ 0 & A \end{pmatrix}$, $A = \begin{pmatrix} -1 & 0 \\ 0 & 1 \end{pmatrix}$, and contain only four distinct eigenvalues in the diagonalization of

the Hamiltonian $\hat{H}^0_{AF}$. Hence we conclude that in the simple one-band Hubbard model, the MSDW state show four energy levels.

The one-particle states are formed by pairing electrons in the four different subbands of appropriate spins, for example, coupling electrons of $\vec{k}\uparrow$, $\vec{k}+\vec{Q_1}\uparrow$, $\vec{k}+\vec{Q_2}\downarrow$ and $\vec{k}+\vec{Q_3}\downarrow$ will give a quasi-particle; or we may choose to couple electrons of $\vec{k}\downarrow$, $\vec{k}+\vec{Q_1}\downarrow$, $\vec{k}+\vec{Q_2}\uparrow$ and $\vec{k}+\vec{Q_3}\uparrow$, and this pairing will give a degenerate quasi-particle.

To diagonalize the 4×4 block Hamiltonian in momentum space and in spin space, we introduce the quasi-particle operator $\gamma^a_{\vec{k}\tau}$ by means of a unitary transformation

$$\gamma^a_{\vec{k}\tau} = U^a{}_{\vec{k}\tau}{}^{a_1}_{\vec{k}\sigma_1} \, a^{\alpha_1}_{\vec{k}\sigma_1}, \qquad a = 0, 1, 2, 3 \tag{3-10}$$

such that

$$\hat{H}^0_{AF} = E^{a_1}_{\vec{k}_1} \gamma^{\dagger a_1}_{\vec{k}_1\tau_1} \, \gamma^{a_1}_{\vec{k}_1\tau_1} \tag{3-11}$$

The degeneracy of $\hat{H}_{AF}$ in Eq (3-9) will manifest itself in the degeneracy in the new spin space τ. The density matrix $\rho^{a\sigma\,a'\sigma'}_{\vec{k}\ \vec{k}}$ will then equal to $U^{a'\sigma'\,a_1\tau_1}_{\vec{k}}U^{a_1\tau_1\,a\sigma}_{\vec{k}} f^a_{\vec{k}}$ with $f^a_{\vec{k}}$ is the Hamiltonian of argument $E^a_{\vec{k}}$. Obviously, the unitary transformation matrix introduced to diagonalize the two 4×4 block matrices is also related by the same similar transformation S.

Again, to simplify the notation, we combine the α index and the spin index into one, such that when the new $\alpha = 0$ we shall mean $(0\uparrow)$, when the new $\alpha = 1$ we shall mean $(1\uparrow)$, when the new $\alpha = 2$ we shall mean $(2\downarrow)$, and when the new $\alpha = 3$ we shall mean $(3\downarrow)$. Similarly $\bar{\alpha} = 0, 1, 2, 3$ will mean $(0\downarrow)$, $(1\downarrow)$, $(2\uparrow)$ and $(3\uparrow)$ respectively. The corresponding (a, τ) and $(a, \bar{\tau})$ are denoted by a and $\bar{a}$. In this simplified notation, the quasi-particle operator will read as

$$\gamma^a_{\vec{k}} = U^{a\alpha}(k)\, a^\alpha_{\vec{k}} \tag{3-12}$$

$$\gamma^{\bar{a}}_{\vec{k}} = U^{\bar{a}\bar{\alpha}}(\vec{k})\, a^{\bar{\alpha}}_{\vec{k}} \equiv \bar{U}{}^{a\alpha}_{\vec{k}}\, a^{\bar{\alpha}}_{\vec{k}}$$

The following section will use this notation exclusively.

4. THE DISPERSION RELATION OF
THE SPIN-WAVE EXCITATION

In the above section, we have already constructed the quasi-particle creation operator $r_{\vec{k}}^{a}$. The AF ground state $|\Phi_0\rangle$ is

$$|\Phi_0\rangle = \prod_{\substack{a,\vec{k} \\ |E_{\vec{k}}^{a}|<E_F}} r_{\vec{k}\uparrow}^{\dagger a} r_{\vec{k}\downarrow}^{\dagger a} |\text{vacuum}\rangle \tag{4-1}$$

and this is the Hartree-Fock ground state.

The collective excited state $|\Psi\rangle_{sw}$ (i.e. the spin wave state) is the superposition of the spin flipping state, in which we destroy an electron in state $(\vec{k}, \alpha)$ of spin σ and create an electron in state $(\vec{k}+\vec{q}, \alpha')$ of opposite spin $\bar{\sigma}$. In other words

$$|\Psi\rangle_{sw} = \phi_{\vec{q}(\vec{k}_1\sigma_1)}^{a_1 \, a_2} a_{\vec{k}_1+\vec{q}\ \bar{\sigma}_1}^{\dagger a_1} a_{\vec{k}_1\sigma_1}^{a_2} |\Phi_0\rangle$$

$$\equiv A_{\vec{q}}^{\dagger} |\Phi^0\rangle \tag{4-2}$$

The ϕ's are the Bloch function as mentioned before. The operator $A_{\vec{q}}^{\dagger}$ is defined by the above equation. We know that the spin wave can take the four wave vectors of $\vec{q}$, $\vec{q}+\vec{Q}_1$, $\vec{q}+\vec{Q}_2$, and $\vec{q}+\vec{Q}_3$; and we shall denote them by $\vec{q}_0$, $\vec{q}_1$, $\vec{q}_2$, and $\vec{q}_3$ respectively.

The Schrödinger Equation for $|\Phi\rangle_{sw}$ will give the following equation for $A^{\dagger}$:

$$\hbar\omega A_{\vec{q}}^{\dagger} = [\hat{H}_{AF}, A_{\vec{q}}^{\dagger}] \tag{4-3}$$

By plugging in $A_{\vec{q}}^{\dagger}$ from Eq (4-2) and the full $\hat{H}_{AF}$ given in Eqs (3-1), (3-2), we shall arrive at an integral equation for $\phi_{\vec{q}(\vec{k}\sigma)}^{\alpha \, \alpha'}$. For nontrivial solutions for the ϕ's, we require that the corresponding determinant will vanish, and this secular equation will give the

$$\det\left\{\mathbf{1} -\mathrm{V}\begin{pmatrix} a_0(0,\,0) & a_0(0,\,1) & -a_0(0,\,2) & -a_0(0,\,3) \\ -a_0(1,\,0) & -a_1(1,\,1) & a_0(1,\,2) & a_0(1,\,3) \\ a_0(2,\,0) & a_0(2,\,1) & -a_2(2,\,2) & -a_0(2,\,3) \\ a_0(3,\,0) & a_0(3,\,1) & -a_0(3,\,2) & -a_3(3,\,3) \end{pmatrix}\right\}$$
$$= 0 \tag{4-4}$$

where $a_\alpha(m,\,n)$ are defined as

$$a_\alpha(m,\,n) = \sum_{\beta_1} \mathrm{L}^{mn}(\vec{q}_{\alpha+\beta_1},\,\vec{q}_{\alpha+\beta_1}) \tag{4-5}$$

with

$$\mathrm{L}^{mn}(\vec{q}_{\alpha+\beta},\,\vec{q}_{\alpha+\beta})$$
$$= \mathrm{U}^{a_1'\,a_1+m}_{\vec{k}_1}\,\mathrm{U}^{\overline{a_1+\beta}\,a_1}_{\vec{k}_1+\vec{q}_{\alpha+\beta}} \times \frac{f^{a_1}_{\vec{k}_1+\vec{q}_0} - f^{a_1'}_{\vec{k}_1}}{\hbar\omega - \mathrm{E}^{a_1}_{\vec{k}+\vec{q}_0} + \mathrm{E}^{a_1'}_{\vec{k}_1}} \times \mathrm{U}^{a_1\,\overline{a_2+\beta}}_{\vec{k}_1+\vec{q}_\alpha+\beta}\,\mathrm{U}^{a_2+n\,a_1'}_{\vec{k}_1} \tag{4-6}$$

Note that the addition of the subscripts on $\vec{q}$ is the same as that for the α's.

5. CONCLUSIONS

In the preceeding sections we investigate the theoretical structure of the MSDW of the γ-Mn system and sucessfully lay down the framework for the calculation of the excitation spectrum of such a system. The excitation spectrum cannot, however, be obtained analytically because we cannot diagonalize analytically the Hamiltonian $\hat{\mathrm{H}}^0_{\mathrm{AF}}$ given by Eq (3-9). We shall diagonalize the $\hat{\mathrm{H}}^0_{\mathrm{AF}}$ by both using the Jacobi's method of sucessive approximation and by using the perturbation calculations. We shall report our progress in a separate paper.

6. APPENDIX A

Figure 2 shows the one-eighth of the original BZ (truncated octahedron) and embedded in the BZ is the one-eighth of the RBZ (a cube). We have drawn only parts of the BZ (positive k_x, k_y, k_z), and the three axes are completely symmetric. Marking the regions outside the RBZ are six small parts.
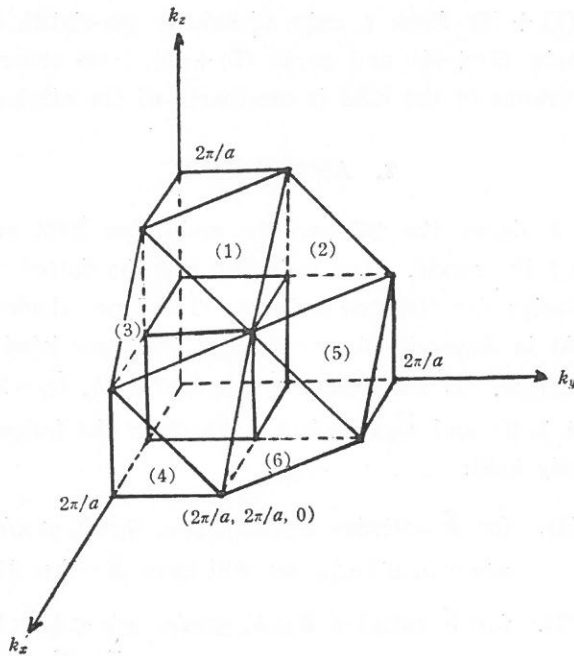
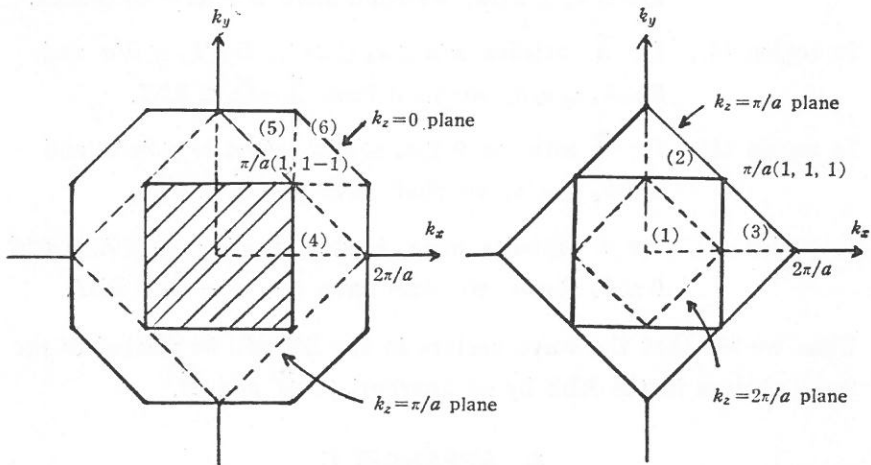Fig. 2. One-eighth of the RBZ is shown here as embedded in the original BZ.

Fig. 3. This figure shows the embedded RBZ as if one is looking along the z-axis. The solid line and the dotted line indicate zone boundaries for different z-planes.

Parts $(1) + (6)$ form a cube of volume one-eighth of the RBZ. Similary parts $(2) + (4)$ and parts $(3) + (5)$ form other two cubes. Hence the volume of the RBZ is one-fourth of the original BZ.

7. APPENDIX B

Figure 3 shows the BZ and the embedded RBZ as if one is looking along the z-axis. The solid line and the dotted line indicate zone boundaries for different z-planes. The inner shadowed area is the RBZ. As in Appendix A, we also use the same label for the six different regions. If we choose $\vec{Q}_1 = 2\pi/a(0, 0, 1)$, $\vec{Q}_2 = 2\pi/a(1, 0, 0)$, $\vec{Q}_3 = 2\pi/a(0, 1, 0)$ and $\vec{G}_0 = 2\pi/a(1, 1, 1)$, then the following results will obviously hold:

In region (1), for $\vec{k}$ satisfies $0 \leq k_x \leq \pi/a$, $0 \leq k_y \leq \pi/a$ and $\pi/a \leq k_z \leq 2\pi/a$, we will have $\vec{k} - \vec{q} \in$ RBZ.

In region (2), for $\vec{k}$ satisfies $0 \leq k_x \leq \pi/a$, $\pi/a \leq k_y \leq 2\pi/a$ and $\pi/a \leq k_z \leq 2\pi/a$, we will have $\vec{k} + \vec{Q}_2 - G_0 \in$ RBZ.

In region (3), for $\vec{k}$ satisfies $\pi/a \leq k_x \leq 2\pi/a$, $0 \leq k_y \leq \pi/a$, and $\pi/a \leq k_z \leq 2\pi/a$, we shall have $\vec{k} + \vec{Q}_3 - \vec{G}_0 \in$ RBZ.

In region (4), for $\vec{k}$ satisfies $\pi/a \leq k_x \leq 2\pi/a$, $0 \leq k_y \leq \pi/a$ and $0 \leq k_z \leq \pi/a$, we shall have $\vec{k} - \vec{Q}_2 \in$ RBZ.

In region (5), for $\vec{k}$ satisfies $0 \leq k_x \leq \pi/a$, $\pi/a \leq k_y \leq 2\pi/a$ and $0 \leq k_z \leq \pi/a$, we shall have $\vec{k} - \vec{Q}_3 \in$ RBZ.

In region (6), for $\vec{k}$ satisfies $\pi/a \leq k_x \leq 2\pi/a$, $\pi/a \leq k_y \leq 2\pi/a$ and $0 \leq k_z \leq \pi/a$, we shall have $\vec{k} + \vec{Q}_1 - \vec{G}_0 \in$ RBZ.

Thus we see that the wave vectors in the BZ will be related to the wave vectors in the RBZ by an appropriate $\vec{Q}$ and $\vec{G}$.

8. APPENDIX C

The spin density wave is defined in Eq $(2-6)$. To facilitate our discussions, we choose the plane wave as the Bloch function. (The

THE OPTICAL PROPERTIES OF ALUMINUM THIN FILMS AND AN INTRODUCTION TO THE THIN FILM LABORATORY

JEN-I CHEN and KUNG-TUNG WU

1. INTRODUCTION

A small but functioning thin film laboratory is being provided for the use of faculty members and graduate students in the Physics Department, serving both teaching and research needs. We herewith introduce the facilities of the laboratory and their functions to those who might be interested.

Thin films have numerous successful applications in science and technology. The techniques for preparing thin films and the instruments required vary greatly, depending on the type of film and the area of application. Our primary goal is focused on researches on optical thin films. The thin film laboratory has two sections—the coating system and the optical measurement system. The coating system is remodeled from a small Leybold pump system. The optical system is a brand new system of double beam spectroscopy for measuring reflectance, transmittance and absorptance of thin films.

The main handicap comes from the pump system. The capacity of the pumping system is simply too small to produce a satisfactory vacuum and to accommodate the heating, rotating and controlling gears in the vacuum chamber. Even without these accessories, the ultimate pressure it can produce is about 10^{-5} torr, not satisfactory for common applications. This greatly limits its applications in preparing thin films. At present, we are trying best to prepare some metal and dielectric films for optical study. We expect that the coating system will give those who are interested sufficient training and experience of vacuum deposition of thin films. We hope that a modern pump system can be acquired in the near future, enabling full use to be made of all the newly acquired equipment.

2. THE COATING SYSTEM

In the coating laboratory, we have the following facilities:

1) The vacuum pump system and vacuum gauges.
2) A 12 kW power supply for thermal evaporators.
3) Crystal thickness monitor and optical interference system for thickness measurement.
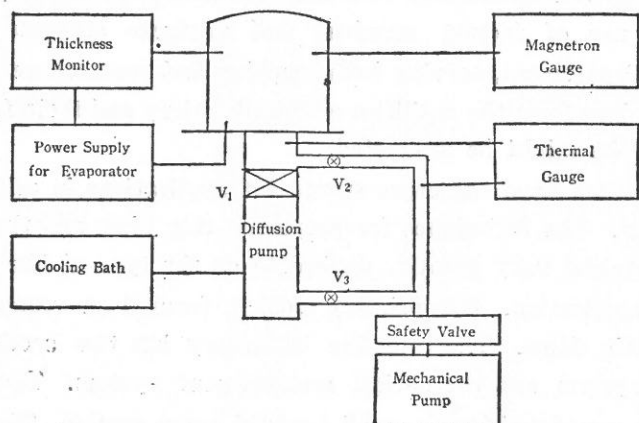4) Ultrasonic cleaner and drying oven.

The arrangement is shown in Fig. 1.

Fig. 1. The Coating System: V_1: high-vacuum valve, V_2: roughing valve, V_3: foreline valve.

The vacuum system is reconstructed from a Leybold pump system (PD 121 EVW/33). Its 60 mm diameter diffusion pump has a pumping speed of only 60 l/sec at 10^{-5} Torr. No liquid nitrogen cold trap is provided. For operations in summer, an additional cooling bath is needed to reduce the cooling water temperature to under 20°C. Because of overheating, the mechanical pump had been replaced by a used CENCO Hyvac 14 with pumping speed 140 l/min at free air. The overheating problem of the safety valve above the mechanical pump was solved by inserting a choke (made from a transformer) of about 0.32 henry to limit its current to a proper value. Both thermal gauge (for 1–10^{-3} Torr range) and Redhead magnetron gauge (10^{-4}–10^{-12} Torr) are Leybold products, purchased

in 1965. In fact, the gauge tube of the magnetron gauge is the last one left, no further supply is possible. The upper structure and all the feedthroughs were made by the machine shop of the physics department, National Taiwan University.

The ultimate pressure of the vacuum system is about 10^{-5} Torr which can be reached after one hour of pumping. The general procedure of operation follows the following steps:[1-3]

1) Open all valves of the cooling loops, put on the cooling bath and set its temperature at 10–15°C.

2) Open the roughing valve, close the foreline valve and the high vacuum valve, and gross pump the vacuum chamber with the mechanical pump for 15–20 min. The pressure will reduce to 4×10^{-2} Torr.

3) Put on the diffusion pump at five minutes after gross pumping starts. It takes about 15 min. to heat up the pump oil. Ten minutes later, close the roughing valve and open the foreline valve, start pumping the diffusion pump for a few minutes. Then open the high vacuum valve and start fine pumping the chamber through the diffusion pump. At this time, it is better to have the high vacuum pressure below 5×10^{-2} torr, since the pumping speed of the diffusion pump is very small above this pressure. Otherwise, gross pump the chamber for another few minutes. About 45 minutes later, the pressure will drop to 10^{-5} torr. It is time for coating.

4) For temporary opening of the chamber, close the high vacuum valve and the roughing valve, keep the mechanical pump and the diffusion pump in stand-by condition; then air the chamber through the airing inlet. One can then lift the bell jar. To start again, put on the bell jar and close the airing inlet, then close the foreline valve and open the roughing valve, and start gross pumping the chamber to below 2×10^{-2} torr. Thereafter close the roughing valve, open the foreline valve and the main valve, and start fine pumping.

5) For over-night or long time rest, close all valves and turn off the mechanical pump and the diffusion pump, while keeping the cooling water running until the diffusion pump oil is handtouchable.

Air cooling by a fan blowing on the lower portion of the diffusion pump is much faster.

6) For first time operation after long time rest, it is better to have the system gross pumped for over one hour.

Precautions of operation: 1) Do not open the foreline valve to the diffusion pump unless the foreline pressure is under 10^{-1} torr. 2) Do not let free air flush the diffusion pump while the oil is still hot. Otherwise oxidation will cause deterioration of the oil.

The thickness of the deposited film is monitored in-process by a crystal thickness monitor (Kronos QM-331). It has a range of $1-2 \times 10^5$ Å and an accuracy to 1 Å. Precaution of operation: The grounding line of 110 V power, the monitor and the vacuum system should be grounded in site. Grounding at the distant main switch is not reliable. Otherwise exaggerated ground loop noise of order 300 mV ppk will cause tremendous trouble and eventually burn the crystal transformer and oscillation electronics.

The readings of the crystal thickness monitor should be calibrated by other methods for each kind of material under each deposition conditon. In our laboratory, this is done by the optical interference method as shown in Fig. 2. The sample is prepared by vacuum deposition. First, a half strip of material of unknown thickness is deposited on a flat substrate, which is subsequently overcoated by a full strip of silver of thickness about 1,000 Å. The sample is put in close contact with a small wedge angle with a reference optical flat of 97% reflectance in the interferometer, which is normally illuminated by collimated monochromatic light. Fizeau fringes are observed through a microscope mounted on a micrometer of 20 cm range and 0.001 mm accuracy. The seperation of fringes and the displacement of fringe across the step are measured with the aid of the micrometer. The thickness of the material film t is given by[1,4]

$$t = \frac{d}{s} \cdot \frac{\lambda}{2}$$

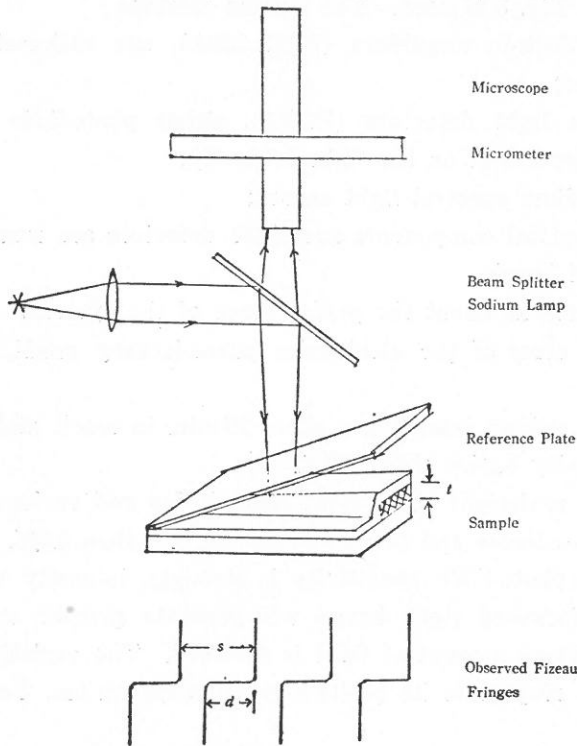where λ is the wavelength of illuminating light.

Fig. 2. Systematic Diagram of Optical Measurement of
Film Thickness.

The parallel between the interference plane and the moving axis of the micrometer is difficult to adjust. This causes observed fringes to drift in time. Also, care must be taken in identifying the connection line of related fringes across the step. This can be done by focussing first on the connection lines. The line width of the fringes can cause an error as large as a few percent. That can be greatly reduced if monochromatic parallel illumination is adopted and the separations of fringes are adjusted to be larger.

3. THE OPTICAL MEASUREMENT SYSTEM

For optical measurements of reflectance, transmittance and absorptance of these films, a double beam spectroscopy arrangement

as shown in Fig. 3 is used. The system includes

1) two lock-in amplifiers (PAR 128A), one ratiometer and a light chopper;

2) three light detectors (D1-D3), either photodiode or photo-transistor, dependent on the light intensity;

3) a sodium spectral light source;

4) all optical components and light detectors are mounted on a micro-optical bench.

Some remarks about the performance of the system:

1) The error of the electronics parts is very small, less than 10^{-4}.

2) The sodium lamp takes about 15 min. to reach stability. Its initial intensity varies about 0.3%.

3) The variations of different photodiodes and various combinations of photodiodes and preamplifiers are less than 0.5%.

4) The photodiode sensitivity is strongly intensity dependent, i.e., better focussed light beams will generate greater output even though the same amount of light is received. The variation of the output with respect to its position is about 7% per cm. For reducing
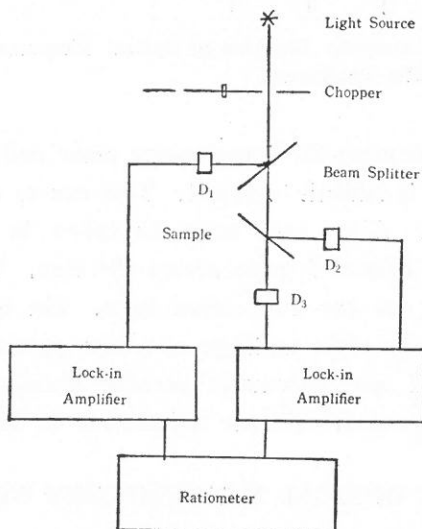
Fig. 3. Systematic Diagram of Double Beam
Optical System.

the large error thus arising, the detectors in reflected and transmitted channels should have the same focussing and be located at strictly the same distance from the reflecting plane.

5) The biggest error comes from the micro-optical bench mounting, which is not rigid enough and often slightly disturbed in changing samples. This affects the reference channel mostly. Also the direction of the reflecting plane of the sample may vary slightly. The overall error arising can be as large as 4%.

3.   THE EVAPORATION OF ALUMINUM AND SILVER[2]

1)   The method of Evaporation

The thermal evaporation techniques are characterized principally by the method used to heat the material to be evaporated. The most common method is that of electrically heated boats or filaments. For the case of evaporation of aluminum, tungsten filaments are used. Tungsten has a limited solubility in molten aluminum, and thus a tungsten heater will not be completely dissolved. The dissolved tungsten does not vaporize at the evaporation temperature of aluminum. In the experiments, we used a tungsten multi-strand helical filament which was made of several strands of tungsten wire twisted together to ensure that molten evaporants which wet refractory metal spirals could be made to flow as a uniform coating over the surface of the heater. The heater wire disintegrates uniformly because the evaporant is evenly distributed over the heater surface. Multi-strand core creates a large surface area for evaporation, and the aluminum is loaded on the core in wire form.

The tungsten filament is connected to a 12 KW power supply. The evaporation power setting $V(1,7)$ supplies a voltage of 6.5 V and current of 70–80 A to evaporate aluminum at the deposition rate of 300 Å/sec at vacuum pressure of 5×10^{-5} Torr. A lower deposition rate of 66 Å/sec can be done by switching the power setting $V(1,4)$ which indicates a voltage of 3.3 V and current of 40–50 A being supplied.

The silver which is used to overcoat aluminum as the reflection layer in the method of Fizeau interference fringes can be evaporated

by the tantalum foil heated boat. At vacuum pressure of 5×10^{-5} Torr, the deposition rate of silver is about 30 Å/sec on the power setting V(1, 4) which indicates a voltage of 3.3 V and current of 180–190 A being supplied.

2) The thickness calibration of deposited films

The geometrical arrangement of the evaporation system is systematically shown in Fig. 4. For the crystal film thickness monitor, the corresponding scaling numbers N for the materials to be deposited are calibrated by the inverse density and corrected for the vacuum system geometry. The numerical setting N is equal to the inverse of material density ρ as well as geometric factor G. That is $N = 1/\rho\, G$. The geometric factor for an evaporation source which approximates a surface source is $G = (r_s/r_t)^2 \cos\theta$, where r_s is the source to
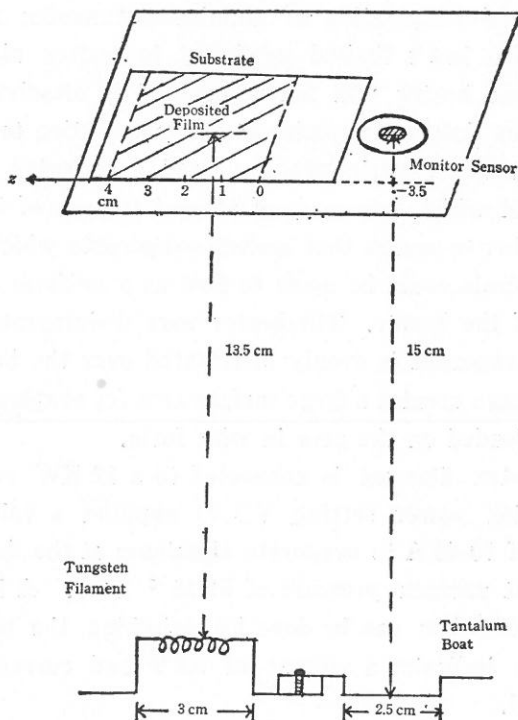
Fig. 4. The geometrical arrangement of the evaporation system.

substrate distance, r_t is the source to transducer distance, and θ is the angle between the normal to the surface of the source and direction of the source to the transducer. First one simply sets the inverse density N as a trial scaling number for the material to be deposited, then deposits a film and reads the thickness display t. The actual thickness as measured by the Fizeau interference fringes method (Fig. 2) is the reading of t'. The correct scaling number is then equal to $N \times t'/t$, and the instrument will be fully calibrated for both geometry and density.

Aluminum has a density of 2.802 gm/cm³ and an inverse density of .370. Set in 370 and deposit a film which is calibrated by the Fizeau interference fringes method. The corrected material scaling number for aluminum is given as $N_{Al} = 522$ at $V(1,7) = 6.5$ V. For silver, the corrected scaling number is given as $N_{Ag} = 182$ at $V(1, 4) = 3.3$ V.

3) The thickness distribution of deposited Aluminum films

The thickness distributions of deposited films have been carefully investigated by the Fizeau interference fringes methods. Fig. 5 shows the distribution of aluminum film along the direction parallel to the filament (ie. z-axis) from which films are being evaporated. Two aluminum films are evaporated at vacuum pressure of 5×10^{-5} Torr and power setting of $V(1,7) = 6.5$ V on the scaling number $N_{Al} = 370$. The corresponding thickness display readings are $t_0 = 3,220$ Å (dotted line) and $t_0 = 3,778$ Å (full line) respectively. The film thickness is maximum in the central 1 cm range because it is directly above the source, and then decreases to both ends, near to or far from the monitor sensor. The irregularity of the lower curve ($t_0 = 3,778$ Å) comes from the foremost evaporation of a nonuniformly distributed aluminum remnant which has already wetted the coil. Films of more uniform thickness can be obtained only if these remnants are completely evaporated off before putting a new charge in uniform distribution and if the filament is kept in position as even as possible.
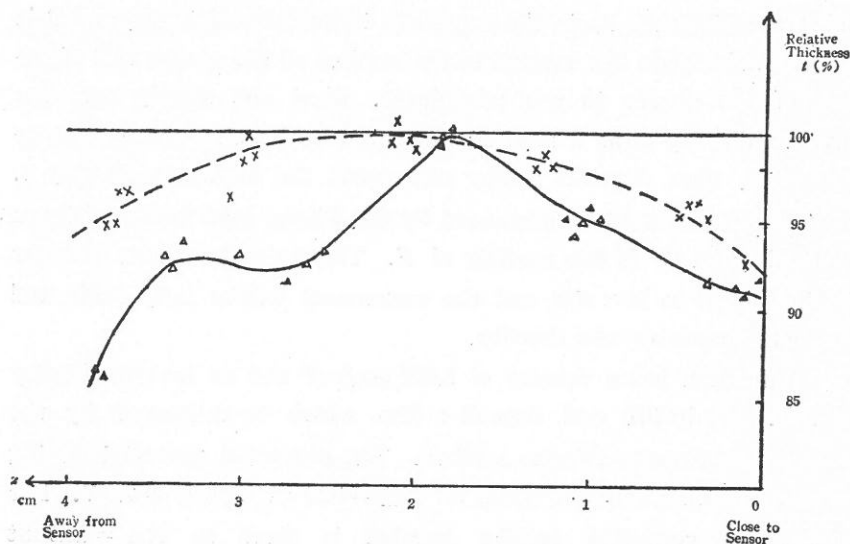
Fig. 5. The relative thickness distribution of Al-film along the direction
parallel to the filament (z-axis). The thickness display readings $t_0 =$
3220 Å (dotted line) and $t_0 = 3778$ Å (full line) are shown.

4. REFLECTIVITY AND TRANSMISSIVITY OF
ALUMINUM FILMS

1) The variations of the transmittance (T), reflectance (R) and absorptance $(A = 1 - R - T)$ of Al-films against thickness

The Al-films of various thickness are prepared in the vacuum
chamber. At vacuum pressure of 5×10^{-5} Torr, two different rates
of deposition are evaporated. The higher one is 300 Å/sec on the
power setting $V(1, 7) = 6.5$ V, and the lower is 66 Å/sec on
$V(1, 4) = 3.3$ V. The substrates are pyrex slides with $n_D = 1.512$ at
room temperature. In each evaporation, Al-films were deposited on
two separate substrates at the same time. After deposition, one of
the films was baked in an oven at 120°C for one hour, and the other
was left unbaked. Their transmittance and reflectance at incidence
of 45° are measured one day later with the double-beam optical
system. The transmittance at normal incidence are also measured.

The logarithm of reflectance of Al-films as a function of thickness

at $\lambda = 5,890$ Å is shown in Fig. 6. The reflectivity of Al-films on glass decreases as the rate of deposition is lowered or the film is baked after deposition. During the evaporation-condensation process, a non-trivial amount of oxygen and other gas is captured or buried by the aluminum condensing on the substrate. This trapping causes increased porosity of the film, and increased surface roughness. This important effect depends on the speed of evaporation (hence, also on the temperature of the source—the independent effect of these two parameters is often not clearly determined). The tendency to form an agglomerated structure is held to a minimum by use of high speed evaporations, combined with low residual pressures. When an Al-film which has been deposited at a normal substrate temperature is baked to 120°C in oven for one hour to induce aggregation, there is only a small decrease in its optical reflection. Increasing the substrate temperature increases the surface mobility of the impinging atoms or molecules, allowing them a greater probability of finding an attractive site, thereby increasing crystallite
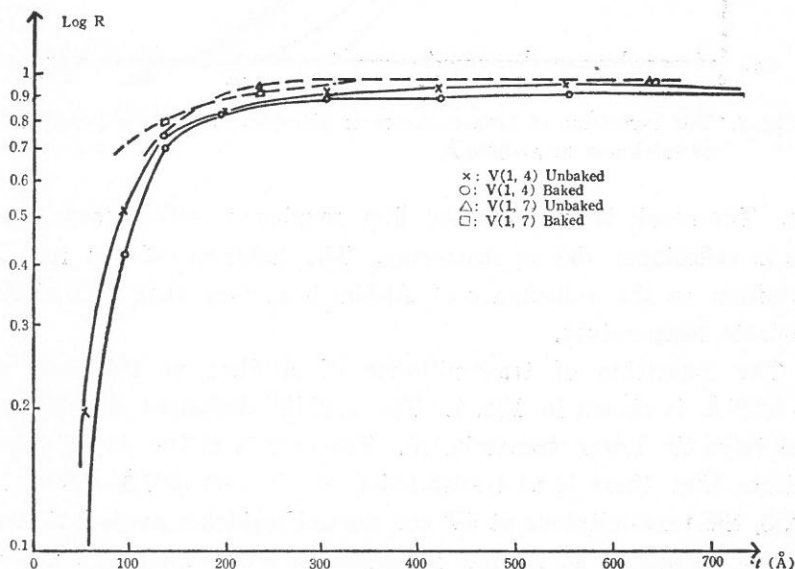
Fig. 6. The logarithm of reflectance of aluminum films as a function of thickness at $\lambda = 5890$ Å.

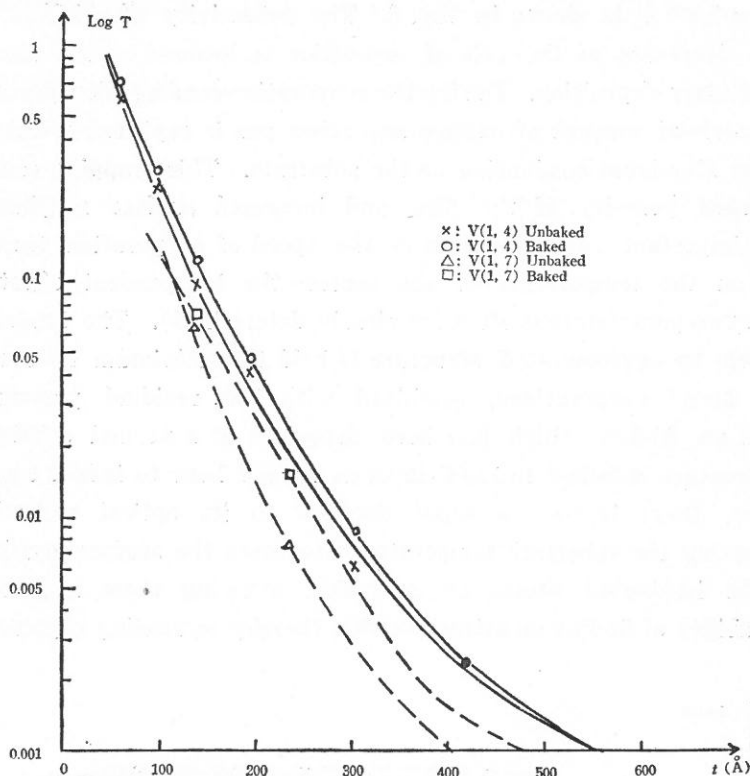Fig. 7. The logarithm of transmittance of aluminum films as a function
of thickness at λ=5890 Å.

size. The result is an increased film roughness with a consequent
loss in reflectance due to scattering. The influence of the rate of
deposition on the reflectance of Al-film is greater than that of the
substrate temperature.

The logarithm of transmittance of Al-films vs thickness at
$\lambda = 5,895$ Å is shown in Fig. 7. The rapidly deposited or unbaked
films have the lower transmission. The results of the experiments
indicate that there is no transmission at all over 800 Å thick. In
Fig. 8, the transmittance at 45° and normal incidence angle is shown.
The transmittance at normal incidence is lower than that at 45°
incidence up to 500 Å. And over 500 Å thick, the transmittance show
very little dependence on the angle of incidence. Fig. 7 and 8

indicate that the decay with thickness in the transmittance is nearly exponential in the range of 50 Å – 300 Å.

The absorptance of Al-films as a function of thickness is shown in Fig. 9. The influence of the rate of evaporation on the optical absorption of Al-film is much greater than that of the substrate temperature. The increased absorptance of the slowly evaporated films is mainly the result of greater oxide contamination of the deposit. For thicknesses of less than 200 Å, the slight increase in optical absorption of the baked film is more likely due to grain growth than oxide contamination. At thicknesses of over 200 Å, the effect of the dependence of absorptance on the baked or unbaked
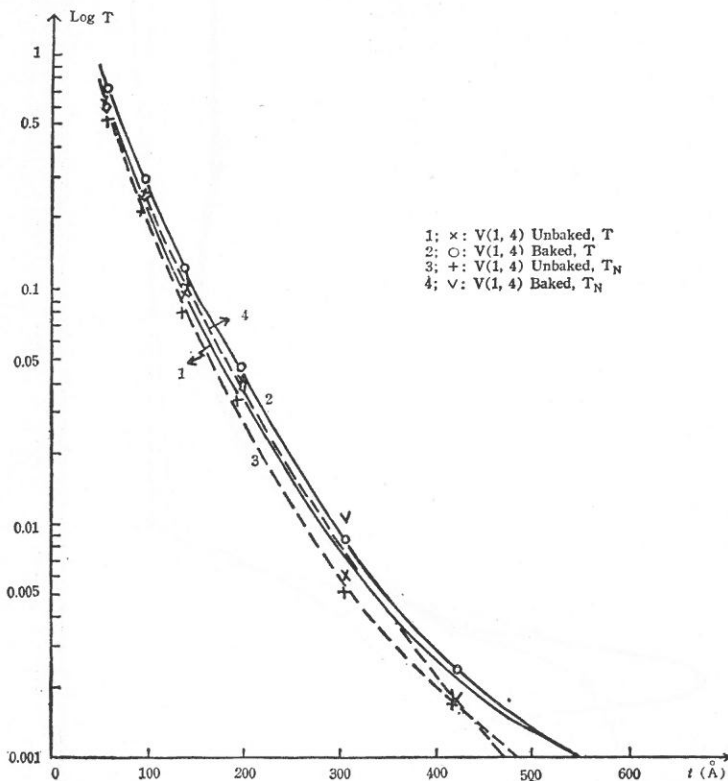
Fig. 8. The logarithm of transmittance of aluminum films as a function of thickness at the incident angles of 45° (T, full line) and at the normal incidence angle (T_N, dotted line).
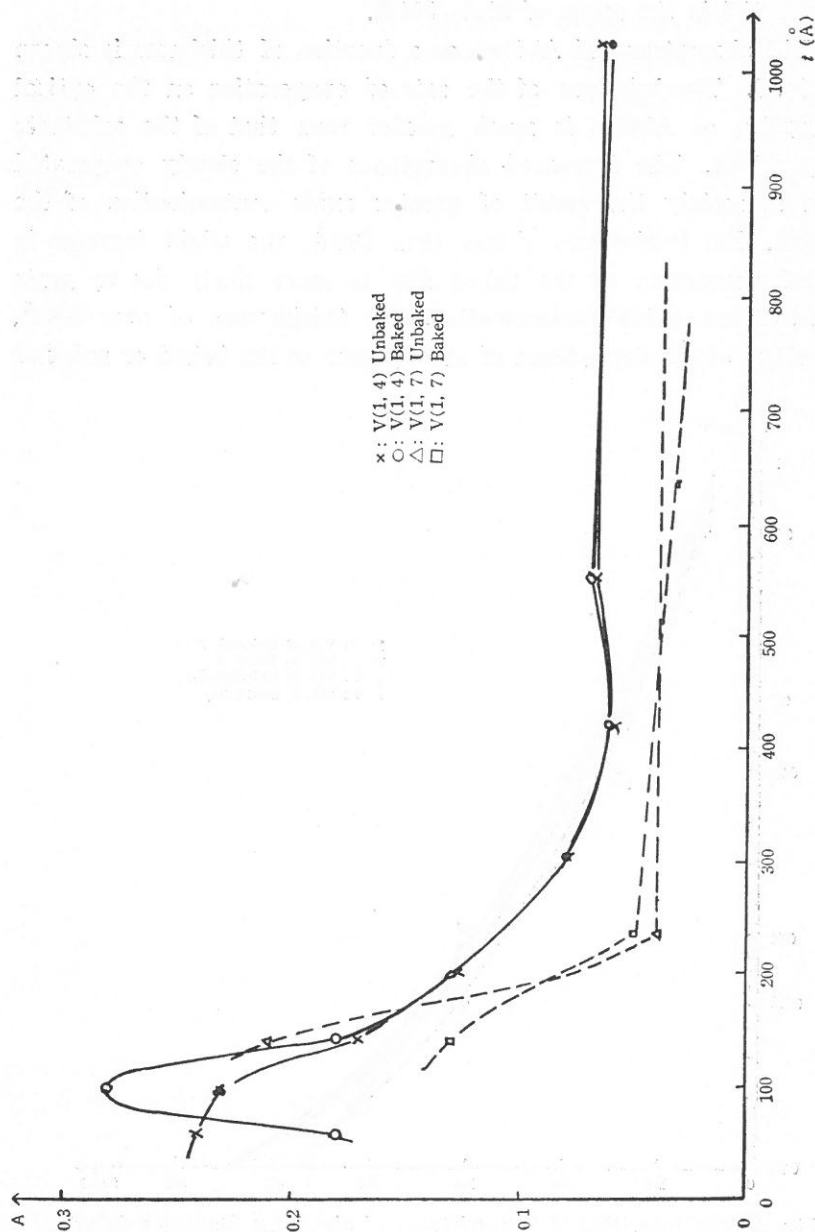
Fig. 9. The absorptance of aluminum films as a function of thickness at $\lambda = 5890\,\text{Å}$.

state of the film becomes unimportant.

In the simultaneous deposition of two films of equal thickness reading, two substrates are put in parallel and the one close to the sensor is baked afterward. In optical measurements, the measuring point of the baked one is at 1 cm position in Fig. 5, while that of the unbaked one at 3 cm position. From the thickness distribution curve (dotted line), one can see that the actual thickness of the unbaked ones are about 1% higher. Which means that all curves for unbaked films in Fig. 6–9 should be shifted accordingly to the left and are almost coincident with corresponding curves of baked films. Therefore after-baking has negligible effect on the optical properties of aluminum film.

2) Discussions

i) A tremendous reduction in reflectance and rise in optical absorption of aluminum films deposited at low rate and high substrate temperature can be expected. But the effect of after-baking is negligible.

ii) In the measurements of the transmittance dependence on the thickness, to avoid the possible error (4%) which may come from optical disturbance of the reference channel affecting the transmittance reading which is already quite small because of highly reflective nature of Al-film, extreme carefulness is needed to reduce the noise.

iii) A lack of 100% reflectance at angles of incidence greater than the critical angle of total reflection can be due to the film having a non-vanishing small absorptance and an oxide or some other contaminating film formed on the surface.

iv) In experiments, a shutter is mounted just above the source. The sample material is evaporated first onto the walls of the chamber and the shutter which is located just above the source to protect the substrate from the evaporating material. Then, after several seconds when the source is fully evaporated, the shutter is opened, exposing the substrate with no interruption of the evaporation. In this way, an accurate deposition rate

and more uniform deposited film is obtained. But when the shutter is closed, some evaporating material still continues to deposit on the substrate causing thickness control problems. This is due to the greater distance between the shutter and the substrate or the thickness monitor sensor. In the forthcoming experiments, we shall improve the situation by mounting the shutter just below the substrate and the monitor sensor.

REFERENCES

(1) Berry, R. W. *et al.*, *Thin Film Technology*, Van Nostrand Reinhold (1968).
(2) Holland, L., *Vacuum Deposition of Thin Films*, Wiley, New York (1956).
(3) *Instruction Manuals for Instruments* (in the Laboratory).
(4) Heavans, O. S., in *Physics of Thin Films*, (G. Hass and R. E. Thun ed.), vol. 2, p. 193, Academic Press (1954).

A STUDY OF SOME EQUATORIAL FARADAY ROTATION RECORDS

JOHN R. KOSTER and YIH-JER TZENG

1. INTRODUCTION

The purpose of this paper is to study a set of Faraday rotation recordings made at Legon, Ghana (lat. 5.6 deg. N; long.–0.19 deg. E) from July, 1978 until January, 1979. These records consist of a series of polarization angle measurements made at 10 minute intervals on the 136 MHz signal radiated by the satellite SIRIO. The satellite was situated in a synchronous orbit at 15 degrees west longitude. Elevation was 71.4 degrees and azimuth was −110 degrees for the Legon observatory. Since 7 years of Faraday rotation data for satellites at low elevations are already available at Legon, we have an opportunity to study the effect of elevation on satellite signals at the equator, and to compare SIRIO results with other data sets. We here confine our study to the sunset to midnight time interval.

The equatorial F-region is an especially difficult one to study, since anomalies abound, and rather spectacular departures from the behavior expected from a normal production-loss-diffusion model of the ionosphere seem to be the rule rather than the exception.

2. THE EEM AND ITS MEASUREMENT

The largest anomalies occur in the hours immediately following ionospheric sunset. It has been found that large plasma "bubbles" are frequently formed in the lower ionosphere (McClure *et al.*, 1977). These bubbles consist of regions in which the electron density may be as much as three orders of magnitude less than that of the ambient medium. They typically rise through the ionosphere, giving rise to large amplitude and phase scintillations of radio signals, "plumes" on the radar power maps made at Jicamarca (Woodman and LaHoz, 1976) and deep minima in TEC measurements made by the Faraday rotation method (Koster, 1973, 1978). The phenomenon
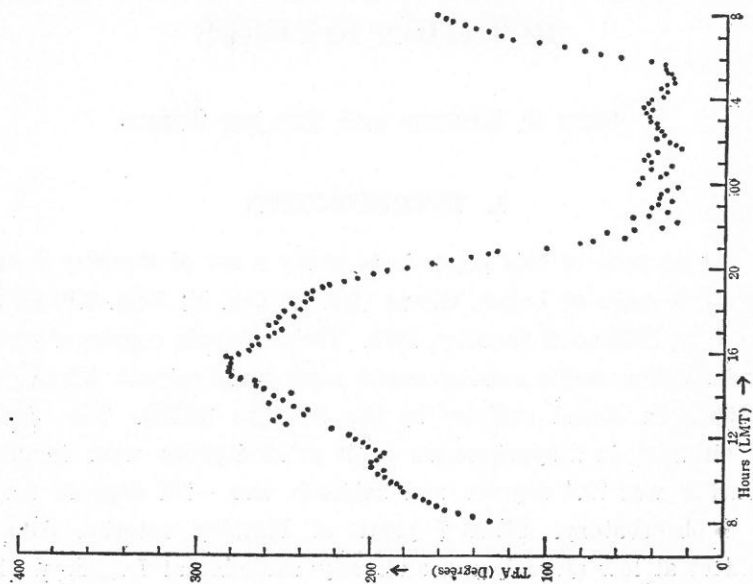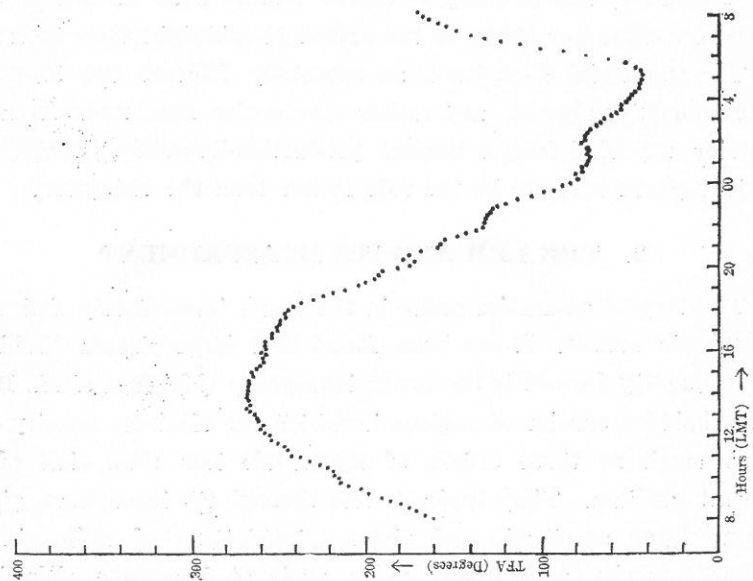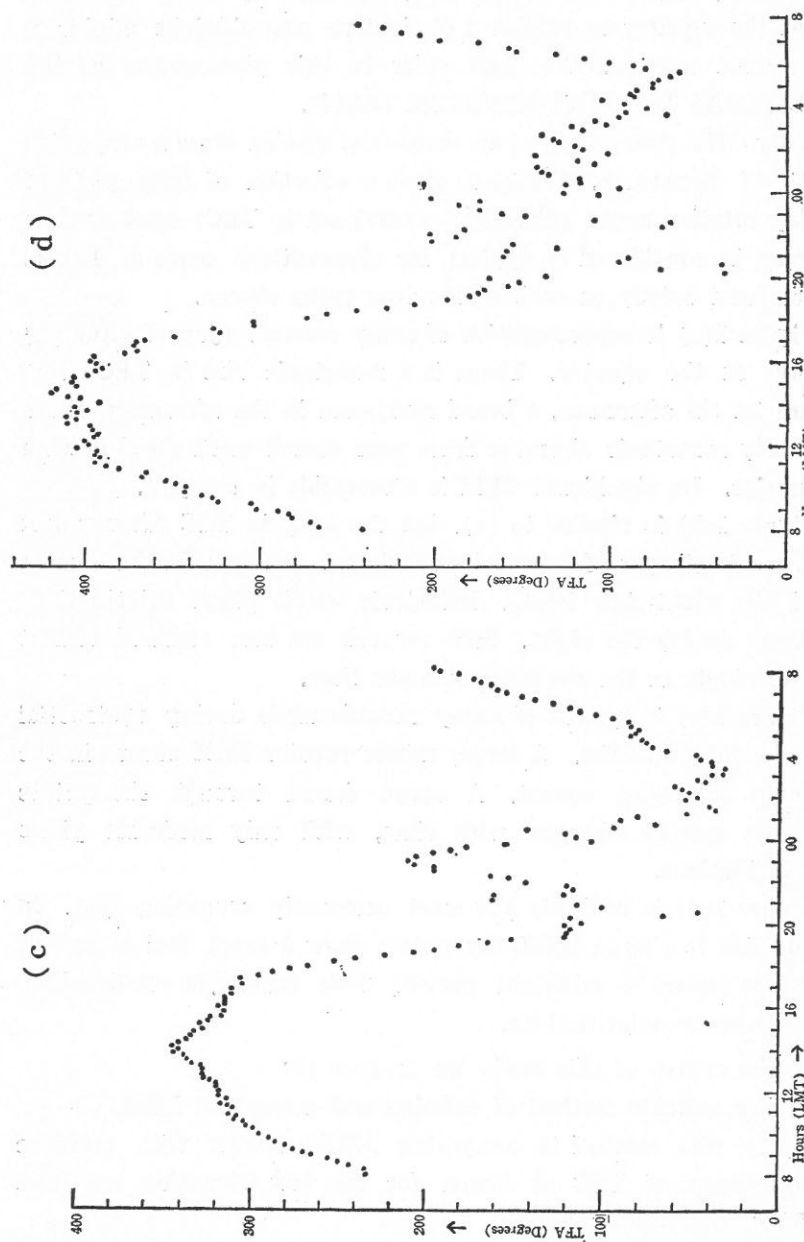
Fig. 1. Plots of total Faraday angle (TFA) as a function of time for four typical days in the Legon SIRIO records. (Further explanation is given in the text.)

is sufficiently regular to cause even the monthly mean values of TEC at the equator to exhibit a distinctive pre-midnight minimum during most months. We shall refer to this phenomenon as the EQUATORIAL EVENING MINIMUM (EEM).

Daily TEC plots made at an equatorial station show a very wide variety of signatures. Figure 1 gives a selection of daily plots of Faraday rotation angle (directly proportional to TEC) against time that may be considered as typical for observations made at Legon. We comment briefly on each of the four types shown.

(a) Figure 1(a) is representative of many summer (June to August) days at the equator. There is a monotonic rise in TEC from sunrise till afternoon, a broad maximum in the afternoon, and a steady monotonic decrease from near sunset until the following sunrise. No significant EEM is discernible in the plot.

(b) Figure 1(b) is similar to (a), but the drop in TEC after sunset is much steeper, followed by an almost constant TEC for most of the night-time hours. Relatively small phase scintillations occur during the night. Such records are also confined almost exclusively to the northern summer time.

(c) Figure 1(c) is typical of many records made during equinoctial and winter months. A large, rather regular EEM occurs in the hours following sunset. A curve drawn through the points shows smooth changes with time, with only moderate phase scintillations.

(d) Figure 1(d) is probably the most commonly occurring type. In addition to a large EEM, the points show a great deal of scatter in the sunset to midnight period. This scatter is attributed to large phase scintillations.

In the course of this study we propose to:

(a) Find a suitable method of defining and measuring EEM.

(b) Apply this method in comparing SIRIO results with previous recordings of TEC at Legon for the low elevation satellites ATS-3 and ATS-5, and

(c) Compare Legon SIRIO results with low latitude but not equatorial records obtained at the same time in the Pacific region.

Figure 1(a) is typical of the type of TEC record obtained at Legon, Ghana during the summer months, when scintillation and EEM effects are at a minimum. The records bear a striking resemblance to the theoretical plots of Nm given by Rishbeth (1963) for the production-loss-diffusion model. These are characterized by a smooth monotonic decrease from a mid-afternoon peak to a minimum near ionospheric sunrise on the following day. We wish to approximate the mid-afternoon to early morning portion of such a curve with some type of analytical function. It has proved feasible to fit a hyperbolic tangent to this portion of the daily curve. A function of the form:

$$y = a + b*\tanh(cx + d)$$

ensures that the monotonically decreasing characteristic is preserved, while the four adjustable parameters can be optimized to give excellent agreement with results such as those shown in Figure 1(a) and 1(b). In our notation we will refer to the values of our original experimental points as Y(I); points on our theoretically fitted curve will be referred to as T1(I). We are interested in studying departures of our experimental points from the smooth hyperbolic tangent. Hence we define a difference function as:

$$DIF1(I) = Y(I) - T1(I).$$

Since this difference may exhibit considerable scatter (due to phase scintillation) as well as a systematic departure from our monotonically decreasing theoretical curve, we wish to remove the scatter by fitting a high degree polynomial (10th degree) to the values of DIF1(I). The points determined from this polynomial are referred to as T3(I).

We are now in a position to give a quantitative definition of EEM. We define EEM as follows:

$$EEM = SQRT(\sum T3(I)**2 / \sum Y(I)**2)*100.0 \quad \text{where:}$$

The summations are taken over points from 18 hours to 24 hours local time.
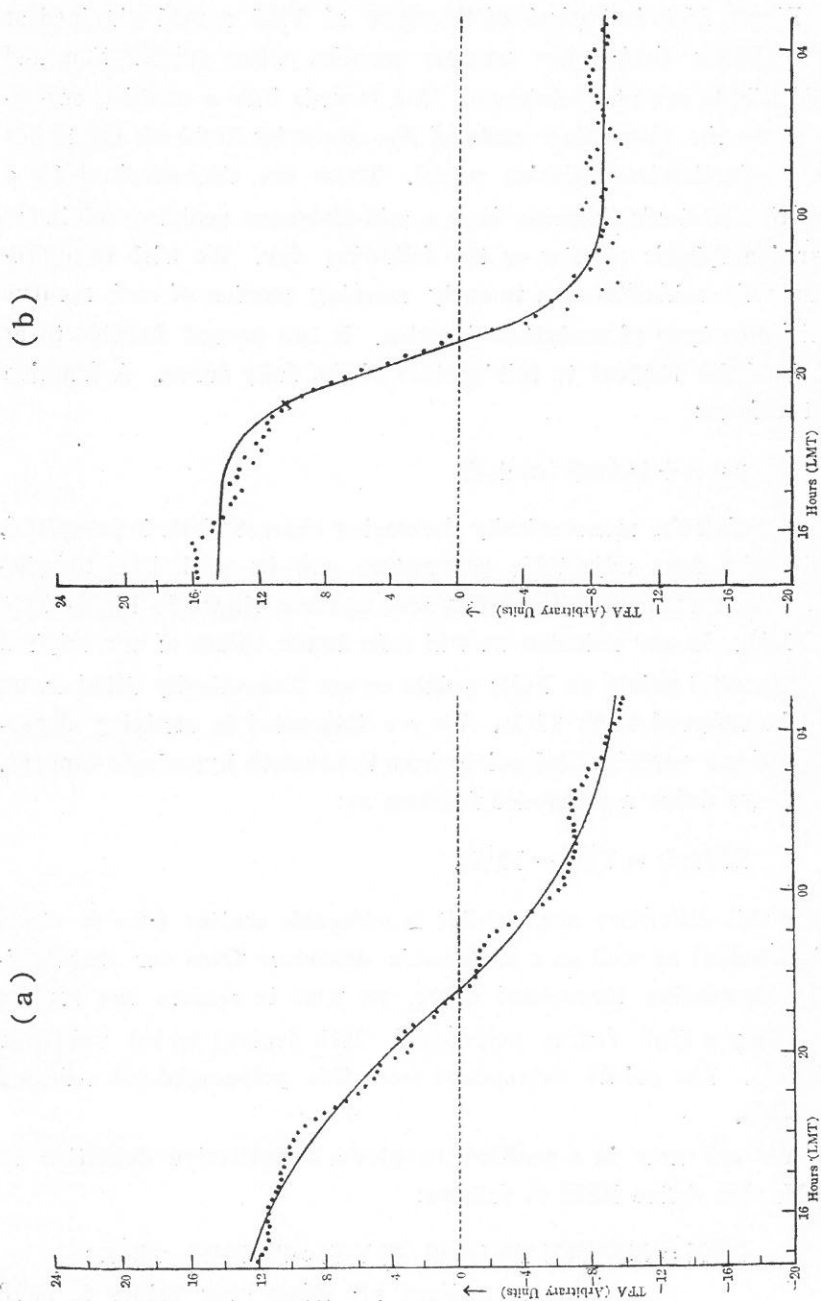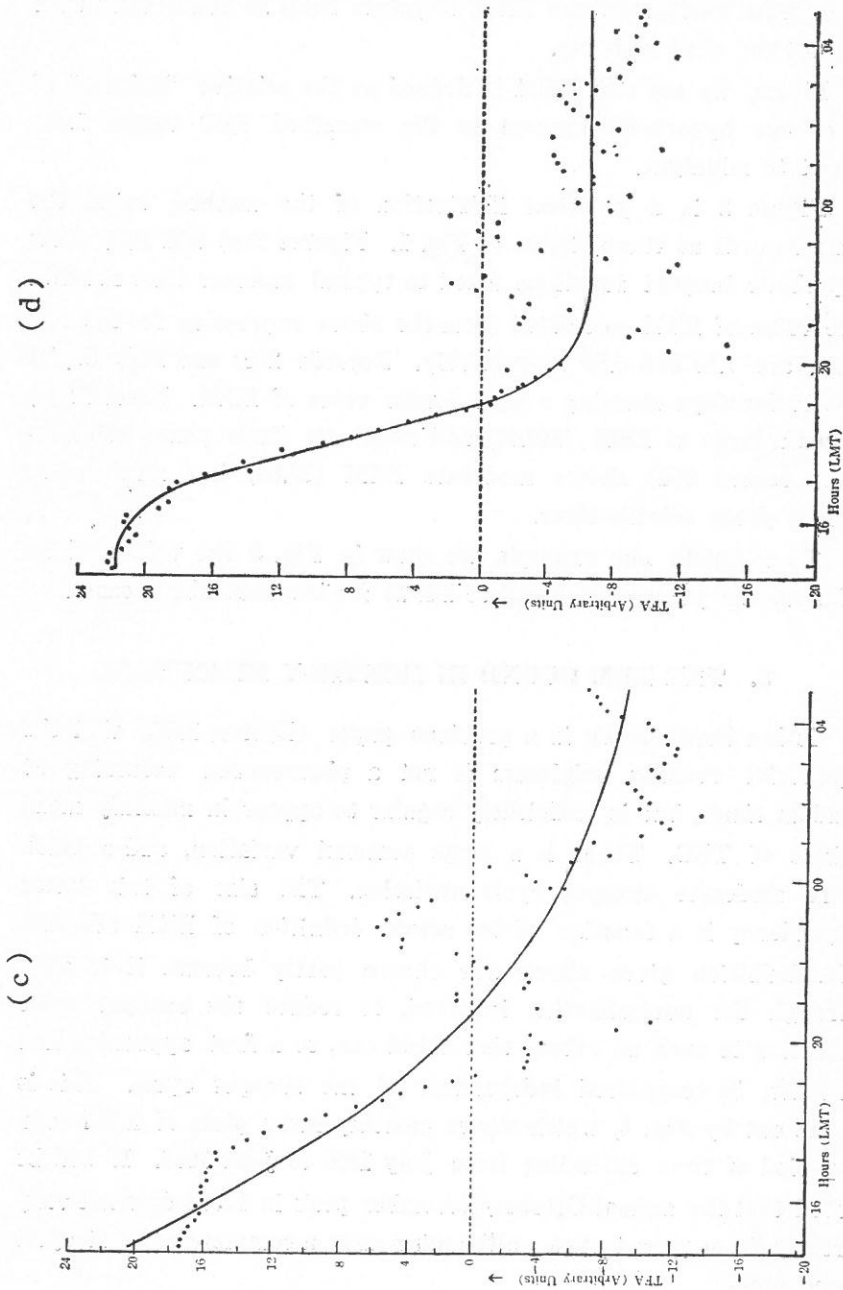
Fig. 2. Best hyperbolic tangent fitted to the records of Fig. 1 for the time interval 14:50 to 05:30 hours LMT.

The curves themselves are fitted to points from 15 hours local time to 05.30 the next morning.

Hence, we see that EEM is defined as the relative "badness" of fit of our hyperbolic tangent to the smoothed TEC values from sunset to midnight.

Figure 2 is a practical illustration of the method, using the same records as those shown in Fig. 1. Figures 2(a) and 2(b) show hyperbolic tangent functions fitted to typical summer time records. The value of EEM calculated from the above expression for the two cases are 7.70 and 6.39 respectively. Records 2(c) and 2(d) depict results for days showing a much larger value of EEM. Record 2(c) shows a large of EEM (107.46) and relatively little phase scintillation; record 2(d) shows moderate EEM (32.84) but much more serious phase scintillations.

To complete our example we show in Fig. 3 the values of T3 (the smooth polynomial fitted to DIF1) for the four above cases.

3. THE EEM FOUND IN MONTHLY MEAN TFA

It has been shown in a previous paper (Koster, 1978) that the equatorial evening minimum is not a phenomenon occurring at random times, but is sufficiently regular to appear in monthly mean values of TEC. There is a large seasonal variation, and a much more moderate sunspot cycle variation. The size of this latter dependency is a function of the actual definition of EEM adopted. The definition given above was chosen partly because it is able, through the normalization involved, to reduce the sunspot cycle variation to such an extent that EEM can, to a first approximation at least, be considered independent of the sunspot cycle. This is borne out by Fig. 4, which shows monthly mean plots of EEM over a period of time extending from July 1969 to June 1978. It will be noted that the annual October/November peak in EEM does not vary greatly from year to year, although nearly a complete sunspot cycle is covered.

The reality of the EEM in monthly mean TEC is confirmed by

the SIRIO results. Figure 5 shows plots of T3 for the seven months of the observations.

We now wish to compare the SIRIO EEM results (elevation=71 degrees) with those obtained with satellites ATS-3/ATS-5 (elevation = 12 degrees). Figure 6 portrays the mean (over 7 years) monthly low elevation results. The error bars represent 1 standard
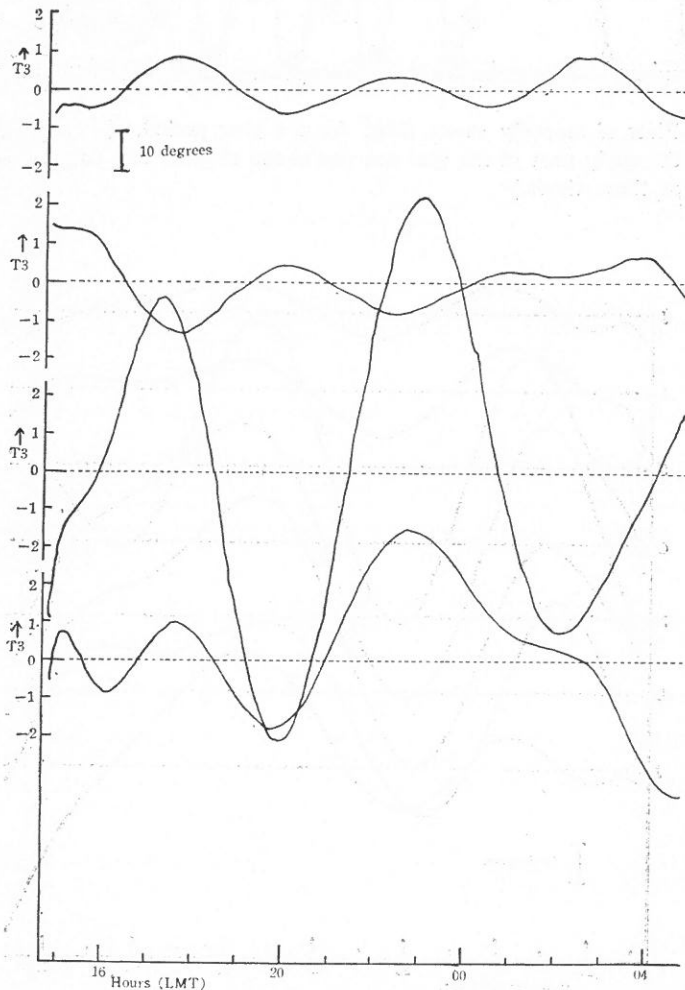

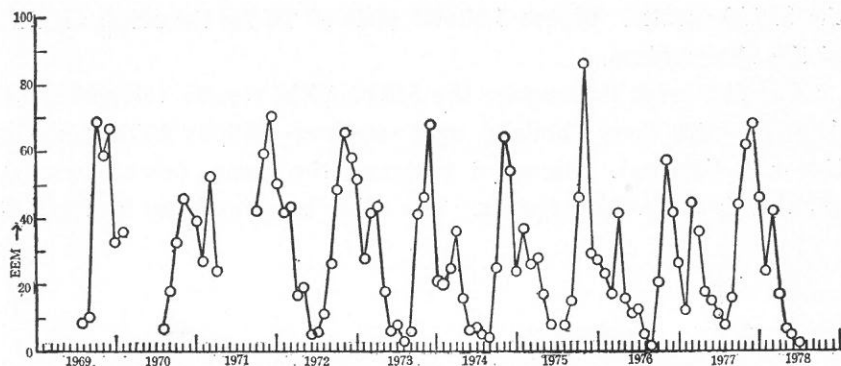Fig. 3. Departures of TFA from the best hyperbolic tangent for the records of Figures 1 and 2.

Fig. 4. Plots of monthly mean EEM for a 9 year period. (The two gaps in the early part of the plot are due to the absence of a suitable satellite at those times.)
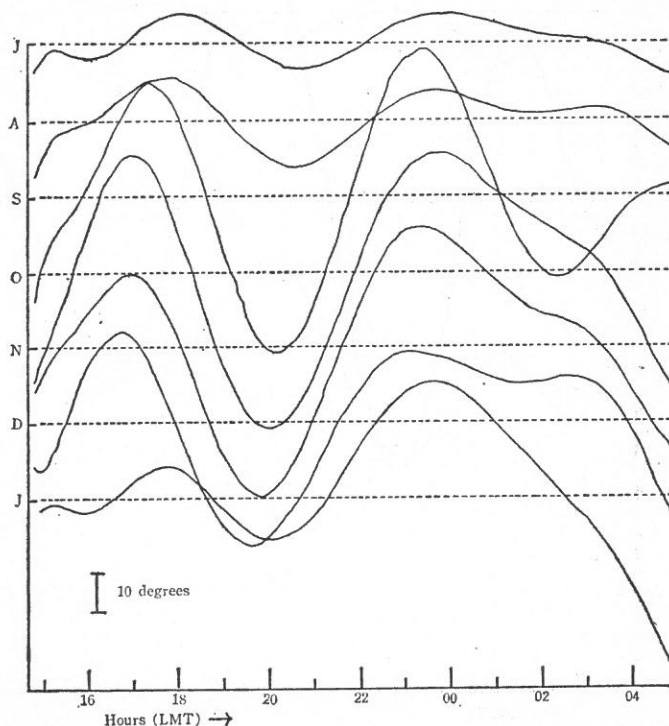

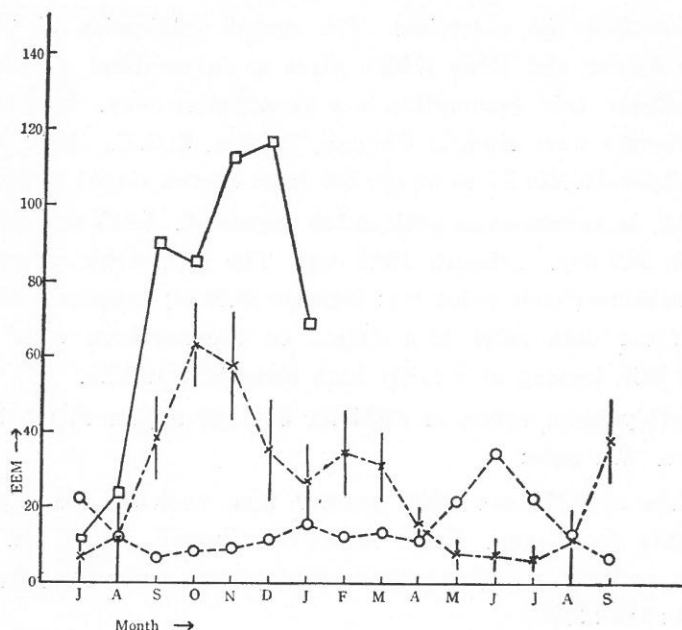Fig. 5. Plots of T3 for the 7 months covered by the SIRIO records at Legon.

Fig. 6. Monthly mean values of EEM for SIRIO (□) at Legon,
ATS-3/5 (×) at Legon, and ETS-2 (○) at Chungli.

deviation above and below the points. The high elevation results
from SIRIO appear on the same plot for comparison. We note the
following points:

(a) All 7 EEM values from monthly mean plots of SIRIO are signifi-
cantly greater than the corresponding values for ATS-3/ATS-5.

(b) The average monthly ratio is 2.16 +/− 0.18.

(c) These data were obtained with the same equipment, at the same
site, and at the same frequency, though at differing times.

Since we have already shown that values of EEM are indepen-
dent of sunspot cycle times, we conclude that EEM is very depen-
dent on satellite elevation from the observing site, large elevation
angles yielding large values of EEM.

4. EEM IN NON-EQUATORIAL TEC RESULTS

We have asserted that the EEM, as defined above, is an equa-
torial phenomenon, but have hitherto given no experimental evidence

to substantiate the assertion. The recent publication of Taiwan TEC by Huang and Chen (1981) gives us an excellent opportunity to investigate this assumption in a quantitative way. The Taiwan measurements were made at Chungli, Taiwan, R. O. C., (latitude 24.95 N., longitude 12..223 E) using the 136 MHz beacon signal transmitted by ETS-2, in synchronous orbit at 130 degrees E. Look angles were: elevation 59.2 deg., azimuth 159.9 deg. The geographic coordinates of the subionospheric point are: latitude 23.03 N; longitude 121.96 E. Hence these data refer to a station on the northern edge of the tropical belt, looking at a fairly high elevation satellite.

Monthly mean values of EEM for Chungli appear at the bottom of Fig. 6. We note:

(a) Values of EEM are much smaller than even the low elevation results for Legon. EEM values for Chungli, Legon low elevation, and Legon high elevation observations are in the proportion 1.00 : 1.96 : 3.99.

(b) The elevation angle was moderately high—hence the small size can hardly be attributed to an elevation dependency of EEM.

(c) There is a significant peak in June, whereas the peak for Legon is in Oct/Nov. It should be recalled that Pacific area scintillation also shows a December minimum and a June maximum.

It is impossible, using these data only, to ascertain how much of this decreased amplitude in EEM can be attributed to the relatively high latitude of the station, and how much is due to a longitude dependency. The matter requires further investigation.

5. TME OF OCCURRENCE OF EEM IN THE MONTHLY MEANS

We have previously defined a variable called T3, which represents the smoothed departure of our actual values of TEC from the hyperbolic tangent fitted to the data. Figures 3 and 5 represent actual plots of this variable as obtained from daily (Fig. 3) or monthly (Fig. 5) plots. We define the time of occurrence of EEM as the time of the largest negative excursion of this variable in the

sunset to midnight time interval. Figure 7 shows a plot of occurrence time of EEM for SIRIO versus E-region sunset time at Legon for the 7 months covered by the data. We note the following:

(a) EEM time of occurrence is strongly correlated with sunset time.

(b) There is a time lag of approximately 1.5 hours. A more precise calculation gives the mean monthly time lag between E-region sunset and EEM time as:

$$t1 = 1.524 + / - 0.039 \text{ hours}$$

Figure 8 shows a corresponding plot of EEM occurrence time versus E-region sunset time for 7 years during which a low elevation satellite was observed. The same trend as that shown above is clearly seen.

For this case we get:
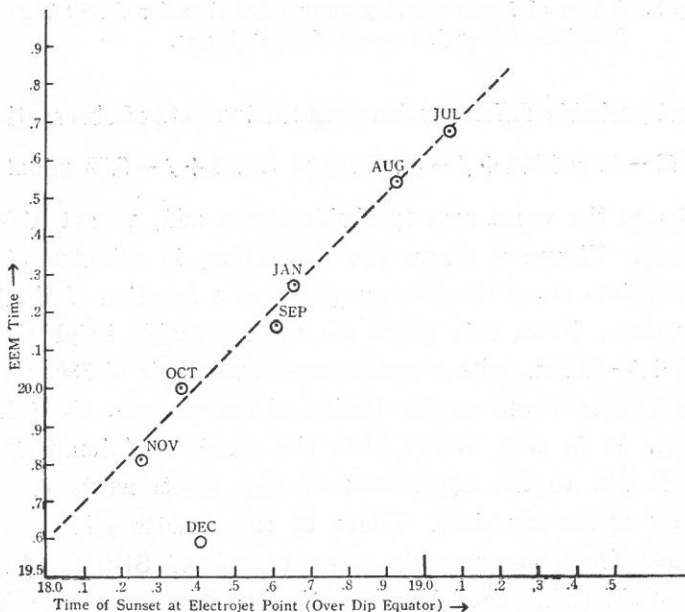
$$t2 = 1.728 + / - 0.045 \text{ hours}$$

Fig. 7. A plot of SIRIO EEM time as a function of E-region sunset time at Legon.
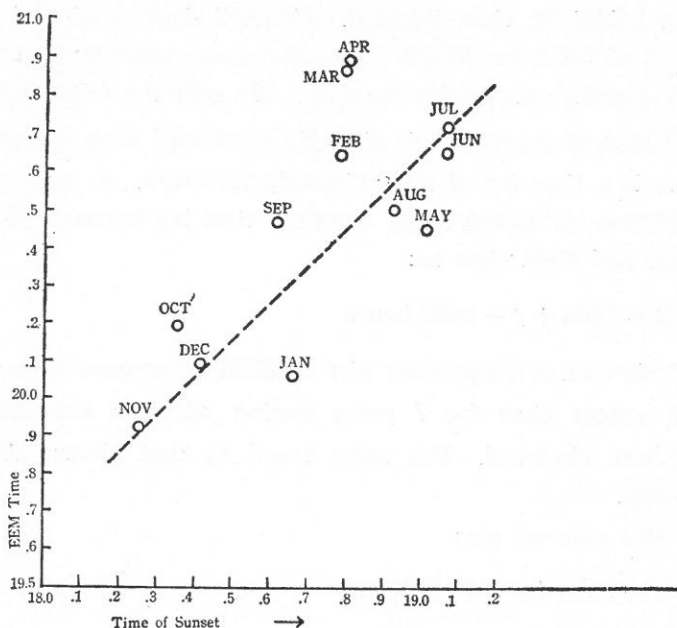
Fig. 8. A plot of 7-year monthly mean EEM time for ATS-3/5 as a function of E-region sunset time at Legon.

The most probable difference between the two sets of observations is:

$$t2 - t1 = 0.204 +/- 0.042 \text{ hours } (12.24 +/- 2.52 \text{ minutes})$$

If we choose the worst case (probable errors add) we get $0.204 +/- 0.084$ hours. Figure 9 shows the separation, in minutes of time, between points along the two ray paths as a function of the height of the points. From this graph our most probable height is found to be $92 +/- 21$ km., with a worst case upper limit of 130 km.

As an extra check on the timing of the records, the following was done. It is well known that the sunrise minimum in TEC records is due to the appearance of new electrons in the upper ionosphere as the sun rises. Times of the sunrise minimum were determined from the monthly mean records of SIRIO and ATS-3. The mean time difference between the two data sets was $0.60 +/- .06$ hours. From Fig. 9 we see that this corresponds to a most probable height of $350 +/- 45$ km. This is in excellent agreement
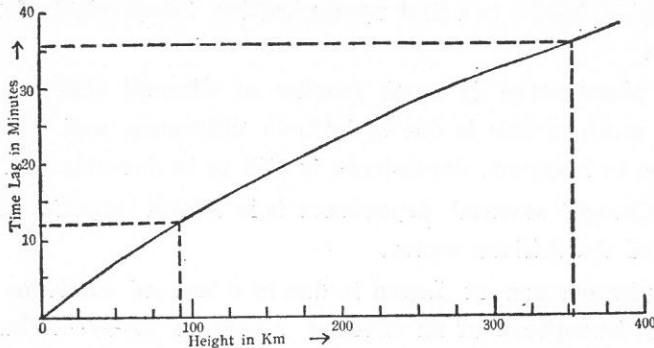
Fig. 9. Time lag in minutes between sunset at points on the line of sight from Legon to SIRIO and ATS-3/5 respectively as a function of the height of the points.

with expectations, and provides additional confirmation that the timing of our records is not in serious error.

We therefore conclude that the effective height of the phenomenon giving rise to the evening minimum is around 100 km. This implies that the evening minimum is mainly due to a loss of electrons in the lower ionosphere, at a height of $92 +/- 21$ km.

6. SUMMARY OF FINDINGS

In this paper we have done the following:

(a) We have given a quantitative definition of the phenomenon which we have called the equatorial evening minimum, and have devised a method of determining its value from TEC or TFA records.

(b) We have shown that the phenomenon is regular enough to be apparent in the monthly mean plots of TEC or TFA.

(c) We have used monthly mean values of TEC to show that the value of EEM obtained at Legon is very dependent on satellite elevation. A satellite at 71 degrees elevation had an EEM value $2.16 +/- 0.18$ times greater than that for a satellite at 12 degrees elevation.

(d) We have shown that the phenomenon has a very large seasonal

variation, but is, to a first approximation, independent of sunspot cycle.

(e) The phenomenon is much smaller at Chungli than at Legon. How much of this is due to latitude difference, and how much is due to longitude dependence is still to be investigated.

(f) The Chungli seasonal dependence is in almost opposite phase to that of the African sector.

(g) The phenomenon at Legon is due to a loss of electrons in the lower ionosphere at an effective height of $92 +/- 21$ km. The morning sunrise minimum is, by contrast, due to electrons at an effective height of $350 +/- 45$ km.

The above results come from the study of the monthly mean values of TEC. The day variability of EEM, as derived from the daily TEC records, is the subject of another study.

7. ACKNOWLEDGEMENT

REFERENCES

(1) Huang, Yinn-Nien and Chen, Sen Wen, Report of the ionospheric total electron content, slab thickness and scintillation observations at Lunping Observatory, January–December 1978, Telecommunications Laboratories, Directorate General of Telecommunications, Chungli, P.O. Box 71, Taiwan, Republic of China, 1981.

(2) Koster, J.R. The equatorial evening minimum in ionospheric electron content. *Fu Jen Studies* 7, 1-14, 1973.

(3) Koster, J.R. the equatorial evening minimum in the total electron content of the ionosphere and its role in equatorial scintillations. Proceedings of the Symposium of the Cospar satellite beacon group, Beacon satellite measurements of plasmaspheric and ionospheric properties. Firenze, Italy, 1978.

(4) McClure, J.P., W.B. Hansen and J.H. Hoffman. Plasma bubbles and irregularities in the equatorial ionosphere. *J. Geophys. Res.* 82, 2650, 1977.

(5) Rishbeth, H., Further analogue studies of the ionospheric F layer, *Proc. Phys. Soc.* (London) **81**, 65-77. (Also treated in: Rishbeth, H., and O. K. Garriott, Introduction to Ionospheric Physics, *Academic Press*, New York and London, 1969)

(6) Woodman, R. F., C. LaHoz, Radar observations of F-region equatorial irregularities. *J. Geophys. Res.* **81**, 5447-5466, 1976.

"I would rather discover one cause
than gain the kingdom of Persia."

DEMOCRITUS

"Jawaharlal Nehru clearly recognized the importance of science. It is due to him that we as a people have at least some consciousness of science. He founded a chain of national laboratories and established what is now the Bhabha Atomic Research Center in Trombay. It was under his inspiration that the Government adopted a Scientific Policy Resolution in 1958.

Science has long ceased to be considered an esoteric pursuit. It has to be part of the life of every Indian, the soldier, the farmer, the worker, the housewife and the student."

INDIRA GANDHI

GAS PHASE PHOTOCHEMISTRY OF CYCLOOCTATETRAENE AND SEMIBULLVALENE
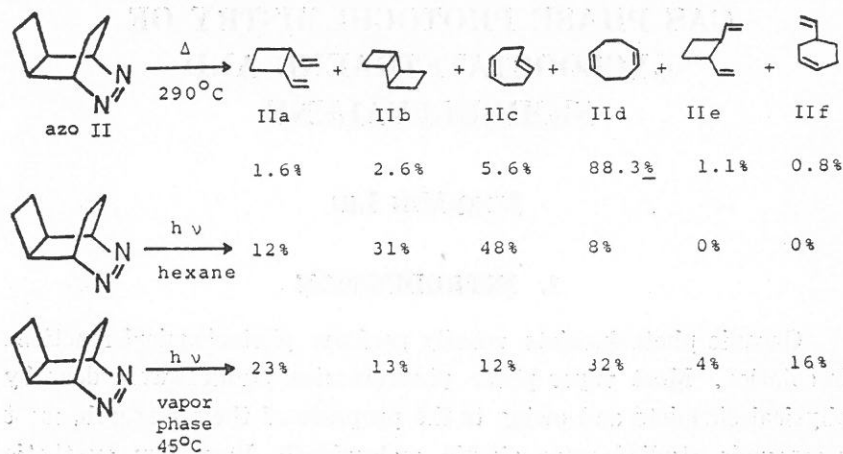
JONQ-MIN LIU

1. INTRODUCTION

Organic photochemists usually perform photochemical reactions in solution. Most vapor phase photochemical studies were done by physical chemists and owing to the purposes of their research, most compounds studied were simple molecules.[1] Very few synthetic chemists would consider vapor phase photolysis as an alternative tool for organic synthesis. However, it has been proven that vapor phase photolysis may be useful in making interesting cage molecules, i. e. vapor phase phase photodecomposition of azo I to produce Ia.[2] (Eq. 1)
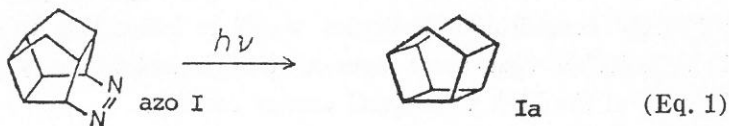
One big difference between vapor phase photolysis and solution phase photolysis is that in the vapor phase the vibrationally excited molecules or diradicals last much longer than those in the condensed phase.[3] It is conceivable that vibrationally excited molecules will behave very differently from molecules in their thermally equilibrated states.

Martin *et al.* have studied azo II by employing a flash thermolysis technique.[4] Two other isomers, IIe and IIf, were found besides the four C_8H_{12} isomers (IIa-d) found in the solution phase irradiation.[5] (Scheme 1)

The formation of IIe and IIf can be explained by the extra activation energy which is provided in the flash pyrolysis but not in the liquid phase photolysis. We found that photolysis of azo II

	IIa	IIb	IIc	IId	IIe	IIf
azo II, Δ 290°C	1.6%	2.6%	5.6%	88.3%	1.1%	0.8%
hν, hexane	12%	31%	48%	8%	0%	0%
hν, vapor phase 45°C	23%	13%	12%	32%	4%	16%

Scheme 1

in vapor phase at 70°C also produced these two isomers and can be explained by the long lifetime of the vibrationally excited diradical intermediate of azo II which contains excess thermal energy.

A conclusion from above is that vapor phase photolysis of relatively complicated molecules would be interesting to study. It is conceivable that some unusual transformations may be found because of the high vibrational energy content.

Semibullvalene is a theoretically interesting molecule. However, its synthesis is not trivial.[6-8] Zimmerman reported a one-step synthesis of semibullvalene (SBV) from cyclooctatetraene (COT), which is an isomer of SBV, by employing low temperature photolysis.[9] The conversion is low and a 5% yield based on 38% unrecovered COT was reported. We have choosen this system to see if gas phase photolysis will give different results or not.

2. RESULTS AND DISCUSSION

We discovered that the vapor phase photolysis of COT at >300 nm resulted in SBV almost quantitatively.[10] (Fig. 1) The vapor phase photolysis of COT was repeated at 254 nm. The major products were benzene and acetylene as reported in the literature.[11-13] The absorption spectrum of COT in the vapor phase is shown

in Fig. 2. COT exhibits a broad weak absorption band with a maximum near 280 nm which tails into the visible region, there is a strong "end absorption", with a shoulder at ca. 305 nm. Yamaguchi reported that the quantum yield of the reaction where COT was decomposed to benzene by light near 254 nm was about 0.1. When the light below 330 nm was cut off by glass filter, COT did not decompose photochemically. They concluded that light below 250 nm was important for the photochemical decomposition. However, our experiments showed that COT underwent rearrangement to SBV instead of decomposition to benzene by irradiating at >300 nm. Wavelength effects on photochemical reactions are known in the literature.[14-16] Our experiment represents another good example.

Semibullvalene was photolyzed at 254 nm at 70°C in the vapor phase. The reaction mixture was analyzed by NMR at different reaction time periods. (Fig. 3) Cyclooctatetraene was found as the primary photoproduct which was decomposed subsequently to benzene and acetylene by absorbing another photon. Polymers were also formed under this condition and were deposited on the wall of the reaction cell. The vapor phase photochemistry of COT is summarized in Scheme 2.[17]
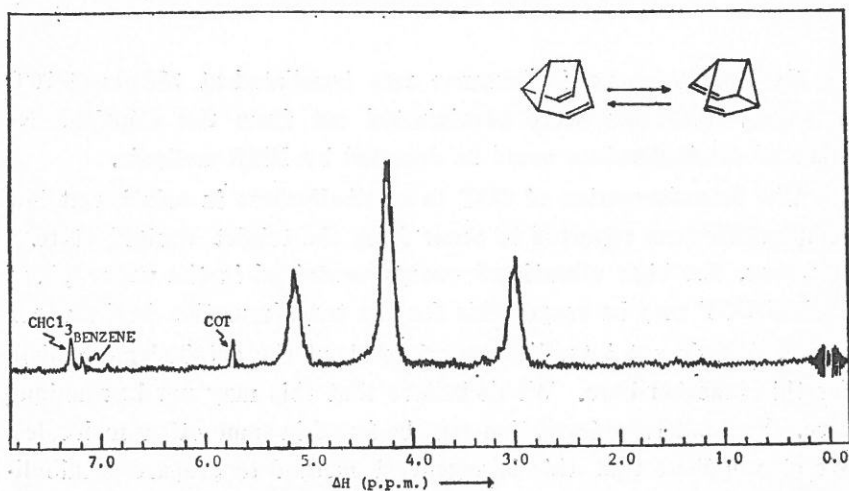

Fig. 1. NMR spectra of the reaction mixture from the vapor phase photolysis of cyclooctatetraene at >300 nm.
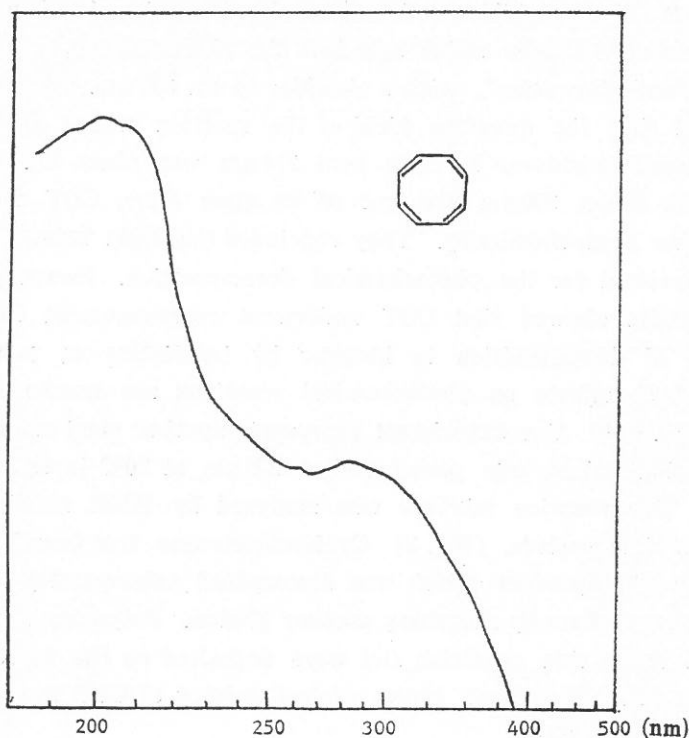
Fig. 2. Absorption spectrum of cyclooctatetraene in the vapor phase.

Cyclooctatetraene in hexanes was irradiated at 350 nm at 70°C and 25°C. Polymers were precipitated out from the solution. No trace of semibullvalene could be detected by NMR analysis.

The transformation of COT to semibullvalene in solution at low temperature was reported to occur from the triplet excited state.[9] However, the high vibrational energy contained in the vapor phase excited COT may be responsible for the transformation in the vapor phase. We do not intend to speculate about the detailed mechanism for this reaction here. We do believe that this may not be a unique case. Unusual transformation may be found in some other molecules. We also believe that this is a general method to prepare semibullvalene derivatives from appropriately substituted COT. This kind of research is currently under way in our laboratory.
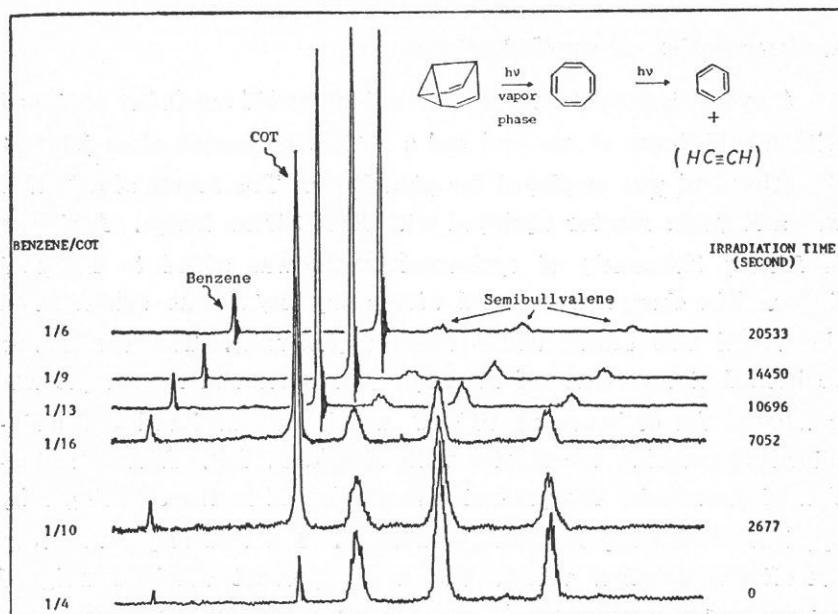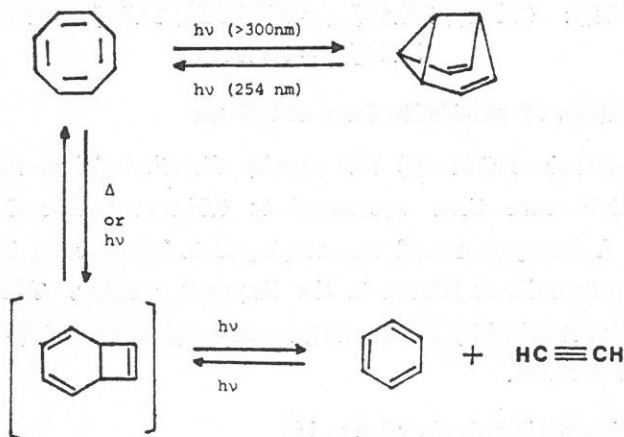
Fig. 3. PMR spectrum of the reaction mixture from vapor phase photolysis of semibullvalene at 254 nm.

Scheme 2

3. EXPERIMENTAL

a. Preparation of semibullvalence

A cylindrical pyrex vessel (24 cm long and 11 cm O. D.) equipped with a cold finger at one end and a ($\mathbb{F}$ 10/30) ground glass joint at the other end was employed for photolyses. The source of radiation was a Rayonet reactor equipped with RPR 350 nm lamps. A charge of 270 mg (2.6 mmol) of cyclooctatetraene was added to the cold finger. The charge was cooled with a dry ice/acetone solution and the vessel was sealed under vacuum (0.05 mm). The vessel was positioned at the center of the Rayonet reactor and the sample was irradiated for 60 hours at $70 \pm 3°C$ which was achieved and maintained by covering the reactor with aluminum foil. After termination of photolysis, the product was condensed in the cold finger by application of a dry ice/acetone solution. The cold finger was then cut off the reaction vessel. The crude product obtained weighed 240 mg and was found by NMR analysis to consist of >98% semibullvalene (90% yield), with traces of benzene (<1%) and COT (<1%).

PMR (CDCl$_3$): (TMS), 5.10 (m, 2H), 4.23 (m, 4H), 3.00 (m, 2H).

CMR (CDCl$_3$): (TMS), 120.8 ($J_{CH} = 164.8$ HZ), 86.7 ($J_{CH} = 169.7$ Hz), 50.2 ($J_{CH} = 153.8$ Hz).

b. Photolysis of semibullvalene at 254 nm

Semibullvalene (100 mg) was equally distributed into five quartz tubes which were then evacuated to 0.01 mm and sealed under vacuum. A merry-go-round was employed to insure even irradiation of the quartz cells at 254 nm in the Rayonet reactor. The reaction mixture was checked by NMR analyses at 0, 2,677, 7,052, 10,696, 14,450, and 20,533 seconds.

c. Gas phase photolysis of azo II

The same as the procedures in a. The mixture obtained was analyzed by vapor phase chromatography (5% OV-17, 70°C.).

REFERENCES

(1) Slater, R.C., Flynn, G.W., *J. Chem. Phys.*, **65**, 425 (1976).
(2) Turro, N.J., Liu, K.C., Cherry, W., Liu, J.M., Jacobson, B., *Tetra. Lett.*, 555 (1978).
(3) Lee, J.C., Lewis, R.S., *Advan. Photochem.*, **12**, 1–98 (1980).
(4) Martin, H-D, Eisenmann, E., Kunze, M., Bonacic-Koutecky, V., *Chem. Ber.*, **113**, 1153 (1980).
(5) Turro, N.J., Liu, J.M., Martin, H-D, Kunze E., *Tetra. Lett.*, 1299, (1980).
(6) Zimmerman, H.E., Bindley, R.W., Givens, R.S., Grunewald, G.L., Sherwin, M.A., *J. Am. Chem. Soc,*, **91**, 316 (1969).
(7) Dauben, W.G., Rivers, G.T., Twieg, R.J., Zimmerman, W.T., *J. Org. Chem.*, **41**, 887 (1976).
(8) Paquette, L.A., Stowell, J.C., *J. Am. Chem. Soc.*, **92**, 5765 (1970).
(9) Zimmerman, H.E., Iwamura, H., *J. Am. Chem. Soc.*, **92**, 2015 (1970).
(10) Turro, N.J., Liu, J.M., Zimmerman, H.E., Factor, R., *J. Org. Chem.*, **45**, 3511 (1980).
(11) Tanka, I., Miyakawa, S., Shida, S., *Bull. Chem. Soc. Japan*, **24**, 119 (1951).
(12) Yamazake, S., Shida, S., *J. Chem. Phys.*, **24**, 1278 (1954).
(13) Yamazake, H., *Bull. Chem. Soc. Japan*, **31**, 677 (1985).
(14) Dauben, W.G., Kellogg, M.S., *J. Am. Chem. Soc.*, **93**, 3805 (1971).
(15) Holovka, J.M., Gardner, P.D., *J. Am. Chem. Soc.*, **89**. 6390 (1967).
(16) Turro, N.J., Rammamurthy, V., Cherry, W., Farneth, W., *Chem. Rev.*, **78**, 125 (1978).
(17) Dudek, D., Glaenzer, K., Treo, J., *Ber. Bunsenges. Phys. Chem.*, **83**, 788 (1979).

"....the primary question was not What do we know,
but How do we know it."

ARISTOTLE to THALES

"It is no paradox to say that in our most theoretical moods
we may be nearest to our most pratical applications."

A. N. WHITEHEAD

CONTRIBUTORS TO THIS NUMBER

Yi-Ching Yen 顏一清 is professor of mathematics at Fu Jen University.

Sheau-Huey Chia 賈小慧 is lecturer of physics at Fu Jen University.

Jen-I Chen 陳振益 is professor of physics at Fu Jen University.

Kung-Tung Wu 吳坤東 is associate professor of physics at Fu Jen University.

John R. Koster, SVD, 高士達 is professor of physics and director of the Computer Center of the College of Science and Engineering at Fu Jen University.

Yih-Jer Tzeng 曾義哲 is a graduate of the Graduate School of Physics at Fu Jen University.

Jonq-Min Liu 劉仲明 is associate professor of chemistry at Fu Jen University.